JGR-Solid Earth, Special Issue 'Ophiolites and Oceanic Lithosphere, with a focus on the Samail ophiolite in Oman', Volume 126, Issue 4, e2020JB020997

doi: 10.1029/2020JB020997

Post-print

Grain size variations record segregation of residual melts in slow-spreading oceanic crust (Atlantis Bank, 57°E Southwest Indian Ridge)

C. Ferrando[1,2,*], L. France[1], V. Basch[2], A. Sanfilippo[2], R. Tribuzio[2], M. Boulanger[1]

[1] Université de Lorraine, CNRS, CRPG, F-54000 Nancy, France.

[2] Dip. di Scienze della Terra e dell'Ambiente, Università degli Studi di Pavia, I-27100 Pavia, Italy.

**Corresponding author*: Carlotta Ferrando, Ph.D. (ottaferrando@gmail.com)

Key Points:

- Geochemical zoning in coarse crystals record crystallization of primitive crystal mush and subsequent reactive melt migration thereof.
- Fine-grained olivine gabbros testify collection of residual melts from the crystal mush; their crystallization is dominated by nucleation.
- Accumulation of migrating melts could have promoted extraction of those melts that potentially contribute to MORB erupted at the seafloor.

Abstract

Beneath slow-spreading ridges, melt bodies are generally considered to represent ephemeral magma reservoirs filled with crystal mushes. Formation of the oceanic crust requires at least partial extraction of melts from these crystal mushes. However, melts collection and extraction are processes yet to be fully constrained. We investigate olivine gabbros from the plutonic section recovered at the IODP Hole U1473A, in the Atlantis Bank Oceanic Core Complex (Southwest Indian Ridge), to unravel (i) the process of melt migration through lower crustal crystal mushes, and (ii) the collection and segregation of melts forming discrete microgabbro intervals. Throughout the Hole, fine- to coarse-grained intervals are widespread in olivine gabbros. Along the contacts, coarse-grained minerals display resorbed grain boundaries against the fine-grained minerals, suggesting partial dissolution by the melt crystallizing the fine-grained material. Coarse-grained plagioclase and clinopyroxene are zoned, showing progressive chemical evolution from more primitive crystal cores to more evolved crystal rims. Fine-grained minerals are unzoned and chemically similar to rims of coarse-grained minerals, indicating a genetic relationship. We attribute significant enrichments in the most incompatible elements of plagioclase and clinopyroxene to a magma evolution process associated with reactive melt migration. As temperature decreased, melts residual from the reactive processes were segregated in magma pockets that ultimately crystallize the fine-grained intervals (microgabbros). We document, for the first time, that those microgabbros are crystallization products of melts modified by reactive melt migration, extracted from the crystal mush and accumulated into discrete melt-rich portions. This process could have promoted partial extraction of those melts that in turn potentially contribute to MORBs erupted at the seafloor.

Keywords: lower oceanic crust; crystal mushes; mineral chemistry; reactive porous flow; melt accumulation and extraction

1. Introduction

Beneath mid-ocean ridge axes, the lower crustal sections are believed to be composed predominantly of crystal mushes (e.g., Sinton & Detrick, 1992; Dick et al., 2008; Gillis et al., 2014; Lissenberg et al., 2019; Boulanger et al., 2020), apparently containing only few percent of interstitial melt. Although meter-thick melt-rich lenses are locally present under fast-spreading centers (e.g., Collier & Singh, 1998; Dunn, et al. 2000; Canales et al., 2009; France et al., 2009), at slow- to ultraslow-spreading ridges such as at the Southwest Indian Ridge, magma lenses were imaged but no steady-state magma reservoirs are believed to persist over the duration of the opening of the ocean (e.g., Sinha et al., 1997; Singh et al., 2006; Jian et al., 2017). Rather, ephemeral magma bodies are considered to exist (e.g., Tucholke et al., 1997; Gracia et al., 1999; Dick et al., 2003). The crystal mush reservoirs are composed of a permeable crystal matrix with melt stored in the pore space, as more generally described for magma chambers at continental magmatic systems (Cashman et al., 2017).

Accretion of slow- to ultraslow-spreading lower oceanic crust is mainly accommodated by tectonic extension involving long-lived detachment faults and exhumation of gabbroic sequences on the seafloor at Oceanic Core Complexes (OCC; e.g., Cannat et al., 2006; Escartín et al., 2008; MacLeod et al., 2009; Blackman et al., 2011). These lower crustal sequences form through a complex history of multiple magmatic intrusions that are emplaced in an actively deforming environment. Magmatic differentiation, driven by fractional crystallization (e.g., Elthon, 1979; Grove et al., 1992; Ross & Elthon, 1997; Villiger et al., 2007; O'Neill & Jenner, 2012; Abily & Ceuleneer, 2013) and *in situ* crystallization (e.g., Langmuir, 1989; O'Hara & Fry, 1996; Coogan & O'Hara, 2015), has been widely considered as one of the predominant processes responsible for the formation of the gabbroic crust. However, melt crystallization can be accompanied by additional magmatic processes that lead to further geochemical complexity during the magmatic evolution, namely *i)* entrapment of melt portions, leading to the formation of chemically evolved crystal rims (e.g., Bédard, 1994; Bédard et al., 2009), and/or *ii)* migration of buoyant and reactive melts through the crystal matrix. The migration of melts, either residual from the crystallization of primitive phases (e.g., Natland and Dick 2001; Lissenberg et al. 2013) or new injections of primitive magma (e.g., Bédard et al., 2000; Leuthold et al., 2014), can trigger partial assimilation of the pre-existing mineral matrix and concomitant crystallization of more evolved phases (e.g., Coogan et al., 2000b; Gao et al., 2007; Lissenberg et al., 2013; Sanfilippo et al., 2015, 2020; Lissenberg & MacLeod, 2016; Boulanger et al., 2020; Zhang et al., 2020). The process of

reactive melt migration is inferred to occur through the connected pores of the crystal mush, and it is thus commonly referred to as 'melt reactive porous flow'. These reactive processes are able to overprint the geochemical records of magmatic differentiation in early crystallized phases and have a strong effect on the composition of migrating melts (e.g., Lissenberg & Dick, 2008).

Whether the formation of abyssal gabbros involves mainly magmatic crystallization of Mid Ocean Ridge Basalts (MORB)-type melts or reactive processes in the lower oceanic crust, they show a typical cumulate geochemical signature (e.g., Dick et al., 2000, 2019; Godard et al., 2009). This indicates that gabbros do not represent frozen MORBs; rather, melts must have been extracted from the crystal mush at some stage of its evolution. Melt extraction is considered to occur by compaction of the crystal matrix (e.g., Natland & Dick, 2001; Solano et al., 2014), although lower crustal gabbroic rocks often record little compaction-driven deformation. The high concentration of interstitial melts into melt-rich zones (assisted or not by compaction) may promote an efficient mechanism to collect the residual melts extracted from the crystal mush (Lissenberg et al., 2019). Numerical modelling of melt transport via reactive flow demonstrate that melt accumulation most likely occurs at the top of the igneous body in reservoirs that contain more than 70% melt, in turn favoring melt mobilization and promoting their eruption (Jackson et al., 2018). The mechanisms of melt extraction from deep crystal mushes at slow-spreading ridges are still poorly constrained, and new constraints are required to shed light on melt aggregation processes giving rise to MORB genesis.

A common feature in oceanic olivine gabbros worldwide is the occurrence of grain-size variations (slow-spreading centers: Atlantis Bank OCC, Dick et al., 1991a, and Atlantis Massif OCC, Mid-Atlantic Ridge, Blackman et al., 2006, 2011; fast spreading centers: ODP Hole 1256D, Teagle et al., 2006; France et al., 2009; Koepke et al., 2011, and Hess Deep, Gillis et al., 2014). At the Atlantis Bank OCC, the micrograbbros were preliminarily interpreted as representing melt transport channels through crystallizing intrusions (Dick et al., 2000); nevertheless, no detailed investigation on their formation process has been conducted yet. To constrain the melt migration and subsequent extraction of the residual melts, we here investigate the 810 m-long in-situ section of lower oceanic crust recently recovered in IODP Hole U1473A at the Atlantis Bank OCC (MacLeod et al., 2017; Dick et al., 2019). In particular, we selected samples of olivine gabbros displaying intense grain-size variations, at different depths throughout the Hole. We perform detailed petrographic characterization and *in-situ* geochemical analyses of mineral phases across grain-size contacts

to comprehend the origin of these grain-size variations. We document that fine-grained olivine gabbro (also referred to as microgabbro) represent *in-situ* crystallized melt-rich levels, which testify former collection of melts possibly residual from reactive porous flow processes.

2. Geological setting and IODP Hole U1473A

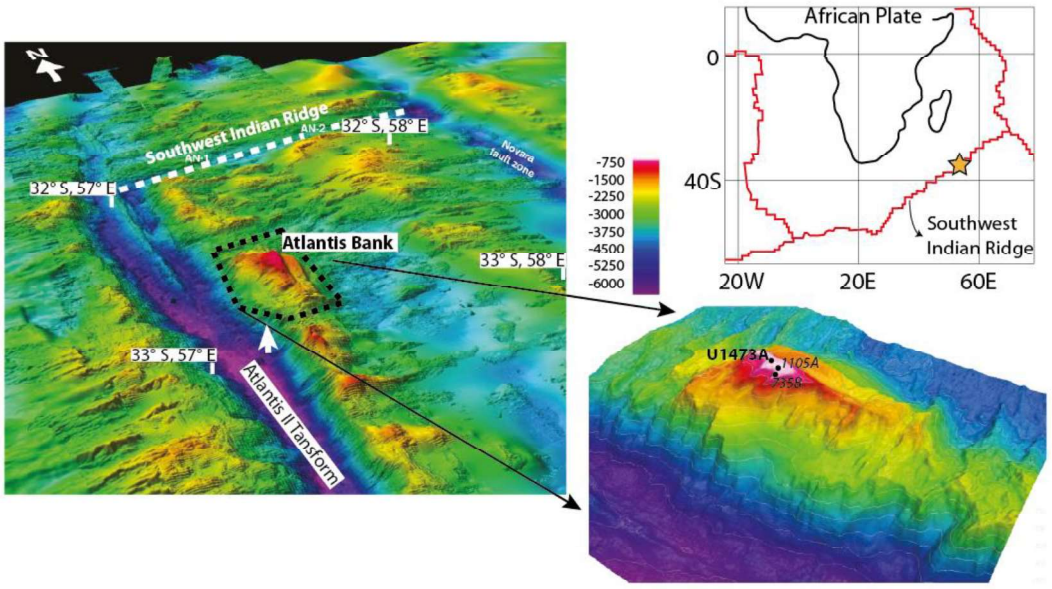

Fig. 1: Location of the Atlantis Bank OCC and detailed 3D reconstruction of its dome structure (looking NE) modified after MacLeod et al. (2017). Holes were drilled on the flat top of the dome. In details, Holes 1109A and 735B were drilled during Legs 118 and 176 of the Ocean Drilling Program (e.g., Dick et al. 2000), and Hole U1473A, studied here, during Expedition 360 of the Integrated Ocean Discovery Program.

The Atlantis Bank, located at 57° E along the ultraslow-spreading SWIR, is a 5 km-high local dome on the eastern wall of the Atlantis II Transform (Fig. 1). This raised dome is an Oceanic Core Complex (OCC) exposing massive gabbro on the seafloor, interpreted to result from initial uplift by detachment faulting at the ridge-transform intersection, and subsequently offset during a period of change in the spreading direction (e.g., Dick et al., 1991b; Baines et al., 2008).

IODP Hole U1473A was drilled during IODP Expedition 360 (Dick et al., 2019) into the flat summit of the OCC, 2.2 km north northeast of the 1508-meters deep Hole 735B (ODP Leg 118 and IODP Leg 176, e.g., Dick et al., 1991a, 2000). This borehole penetrated ~810

meters below sea floor (mbsf), recovering a section of lower oceanic crust (Fig. 2) mainly composed of olivine gabbros (76.5 %), less abundant disseminated-oxide gabbro (containing 1–2% oxide; 9.5% of recovery), oxide gabbro (>5% oxide; 7.5% of recovery), and gabbro (*sensu stricto*; 5% of recovery), and minor felsic veins (1.5%). Two major chemical discontinuities were identified downhole by Shipboard bulk rock analyses (at ~60–90 mbsf and ~350 mbsf, MacLeod et al., 2017), separating three principal chemical units. Each chemical unit is characterized by gradual upsection decreases in Mg# (Fig. 2), Ca#, and Cr and Ni bulk concentrations coupled with increase in Ti and Y contents, similar to chemical trends observed throughout the nearby ODP Hole 735B (Dick et al., 2000). According to Dick et al. (2000), the chemical units in Hole U1473A are interpreted as upward differentiated magmatic intrusive units.

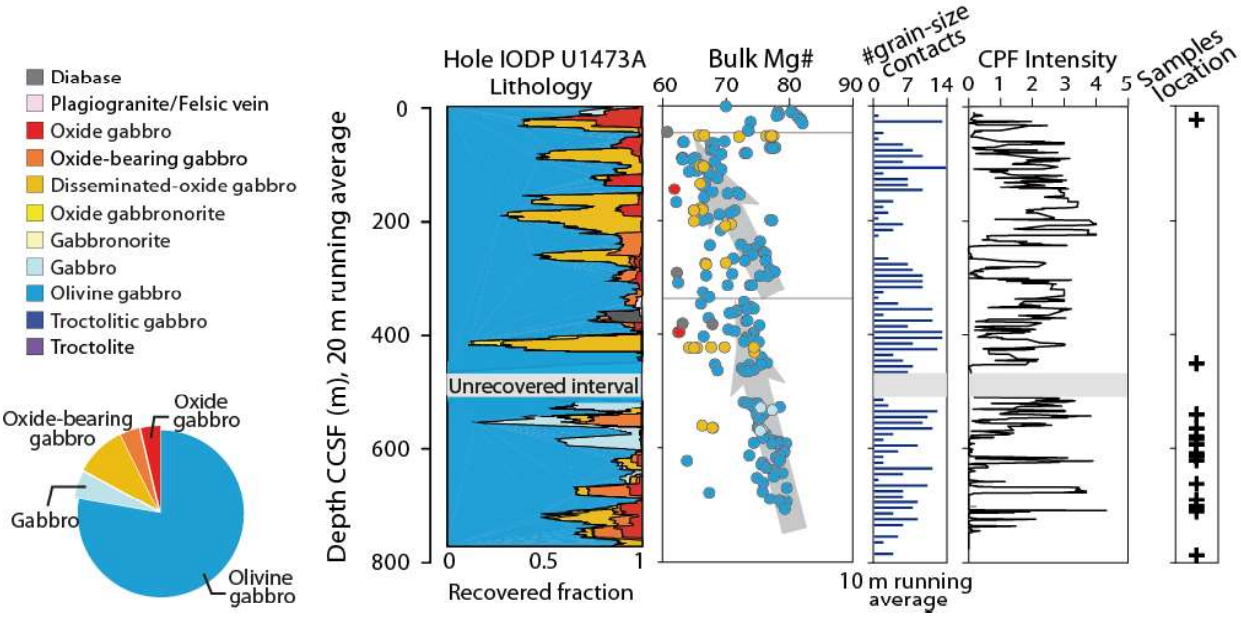

Fig. 2: (from left to right) Pie diagram showing lithologic proportions (vol%) in Hole U1473A; downhole lithostratigraphic variations (relative abundances of rocks are averaged over 20 m) and bulk-rock Mg# (Mg# = 100 × cationic (Mg/(Mg+ Fe), with all Fe as Fe2+) of the recovered samples; number of grain size contacts averaged over 10 m; downhole intensity of crystal plastic fabrics; depth of selected samples.

Grain-size of olivine gabbros is highly variable ranging from coarse- to medium- and fine-grained. About 80% of recovered olivine gabbros are coarse-grained, while the remaining 20% are medium- and fine-grained. Primary contacts between intervals of different grain-sizes are copious (121 contacts according to MacLeod et al., 2017; one contact on average every ~4 m of recovered core) and were identified throughout Hole U1473A at all depths (Fig. 2). Grain-size variations are mostly irregular and “patchy”, i.e. showing coarse-grained

domains included into a fine-grained matrix, with variable thickness of fine- (or medium-) and coarse-grained intervals (Fig. 3; MacLeod et al., 2017). More rarely, the grain-size contacts are sharp, planar and subparallel boundaries that define local igneous layering (Dick et al., 2019). Overall, grain-size contacts are more abundant in the deepest chemical unit (300-800 mbsf; Fig. 2) with on average one contact every ~1.5 m.

Throughout Hole U1473A, primary structures and textures are typically variably overprinted by deformation and crystal-plastic fabrics (CPF). The intensity of CPF decreases downhole: between 550 and 800 mbsf primary grain-size variations are well preserved (Fig. 2). The strong CPF overprint of the shallowest part of the Hole likely partially prevents the identification of additional grain-size variations.

3. Sample selection and analytical methods

During IODP Expedition 360, cutting of rock pieces was performed perpendicular to the foliation plane (when visible) and possibly perpendicular to the orientation of grain-size contacts, ideally maximizing the expression of dipping structures on the cut face of the core (MacLeod et a., 2017). Therefore, the observed irregular shapes of grain-size contacts do not represent 2D-cutting artefacts but are rather real natural features. We sampled fine- and coarse-grained olivine gabbros displaying irregular grain-size contacts at variable depths throughout Hole U1473A. A total of 28 samples were selected: 16 samples across the grain-size contacts and 6 couples (12 samples) within single grain-size intervals, each sampled at 2 to ~20 cm distance from their respective grain-size contact (Table S1). Of the considered 22 grain-size contacts, 9 are visually sharper and 13 are difficult to delineate and more irregular (*Type 1* and *Type 2*, respectively, as detailed in the following). Representative samples were selected in the least deformed and least altered intervals of the hole and thus mainly within the deepest chemical unit (Fig. 2). For comparison with contacts in the upper unit of Hole U1473A, we also sampled a contact at 24 mbsf (360-U1473A-4R-2W, 19-27) and a couple of fine- and coarse-grained olivine gabbros each sampled at ~5 cm distance from their contact located at 450 mbsf (360-U1473A-50R-1W, 73-80 and 360-U1473A-50R-1W, 92-97).

In situ mineral major and trace element analyses were performed across grain-size contacts. We investigated the systematic changes of olivine, plagioclase and clinopyroxene

chemical compositions from the contact into each grain-size interval at increasing distance from the contact.

Minerals major element analyses were performed by Electron Probe Micro Analyzer (EPMA) at Géosciences Montpellier (University of Montpellier), using a CAMECA SX100 equipped with five wavelength-dispersive X-ray spectrometers (WDS). Analyses were conducted with 20 kV accelerating potential, 10 nA beam current and 30 s counting time for all elements measured. Natural minerals and synthetic oxides were used as standards.

Minerals trace element compositions were determined at Géosciences Montpellier, using a Thermo Scientific Element 2XR (eXtended Range) high resolution - Inductively Coupled Plasma Mass Spectrometer (ICP-MS). The ICP-MS is coupled with laser ablation (LA) system, a Microlas (Geolas Q +) automated platform with a 193 nm Excimer Compex 102 laser from LambdaPhysik. The laser energy density was set to 12–15 J cm^{-2} and ablation frequency to 10 Hz for analyses of olivine and 8 Hz for plagioclase and clinopyroxene. The laser spot size was set to 77-85 µm. Data were reduced with the GLITTER software package (Van Achterbergh et al., 2001), using the linear fit to ratio method. Concentrations were calibrated against the NIST 612 rhyolitic glass using the values given in Pearce et al. (1997). ^{29}Si for olivine and ^{43}Ca for plagioclase and clinopyroxenes were used for internal standardization relative to EPMA data. Instrument sensitivity related to analytical conditions was determined from the average across all days of repeat measurements of NIST 612. Detection limits were <15 ppm for Ca, between 0.15 and 0.8 ppm for Ti, Cr, Ni and Zn; they were <65 ppb for Mn and Cu, and <25 ppb for Sc, V, Co. Detection limits for the most incompatible elements were <5 ppb except for Rb, Sr and Ba (<10 ppb). Reference basalt BIR-1G was used as standard to monitor accuracy as well as reproducibility within single series and between runs. This resulted in reproducibility better than 5% for V, Co, Cu, Sr, Nb, Sb, Ba, REE and it is <15% for all other elements.

4. Contact characteristics and textures in olivine gabbros

4.1 Irregular grain-size contacts

The irregular and patchy grain-size variations investigated in this this study are characterized by: *(i)* sutured grain-size contacts that are not planar and display variable orientation (Fig. 3a,c), and *(ii)* variable thickness of coarse-grained domains embayed in fine-

grained olivine gabbro. Based on the thickness of coarse-grained intervals, we distinguish two types of these irregular grain-size contacts that are ubiquitous throughout Hole U1473A and show no systematic distribution downhole (Fig. 2 and Table S1).

Type 1 are characterized by coarse-grained intervals (grain size > 4 mm) up to ~60 cm-thick (thickness is estimated considering studied samples only) in contact with variably thick (<20 cm) intervals of medium- (grain size = 1-3 mm) to fine-grained (grain size < 1 mm) olivine gabbro (Fig. 3a). Fine-grained domains are minor in comparison with more common medium-grained intervals. Contacts are sharp but wavy and lobate (Fig. 3b).

Type 2 present medium- to fine-grained intervals up to 50 cm-thick, but locally reaching only 2-3 cm-thick, in contact with coarse-grained intervals. The coarse-grained olivine gabbro is locally embayed within the fine-grained intervals in levels less than 10 cm-thick, forming 1 to 2 cm-thick patchy coarse-grained domains (Fig. 3c,d). Sparsely, single crystals of coarse-grained olivine, plagioclase or clinopyroxene are isolated within fine-grained olivine gabbro. The contacts are often difficult to delineate as the medium- to fine-grained minerals locally appear to crystallize between the coarser-grained minerals (Fig. 3d).

Hereafter, both medium- and fine-grained crystals and olivine gabbros are referred to as 'fine-grained'.

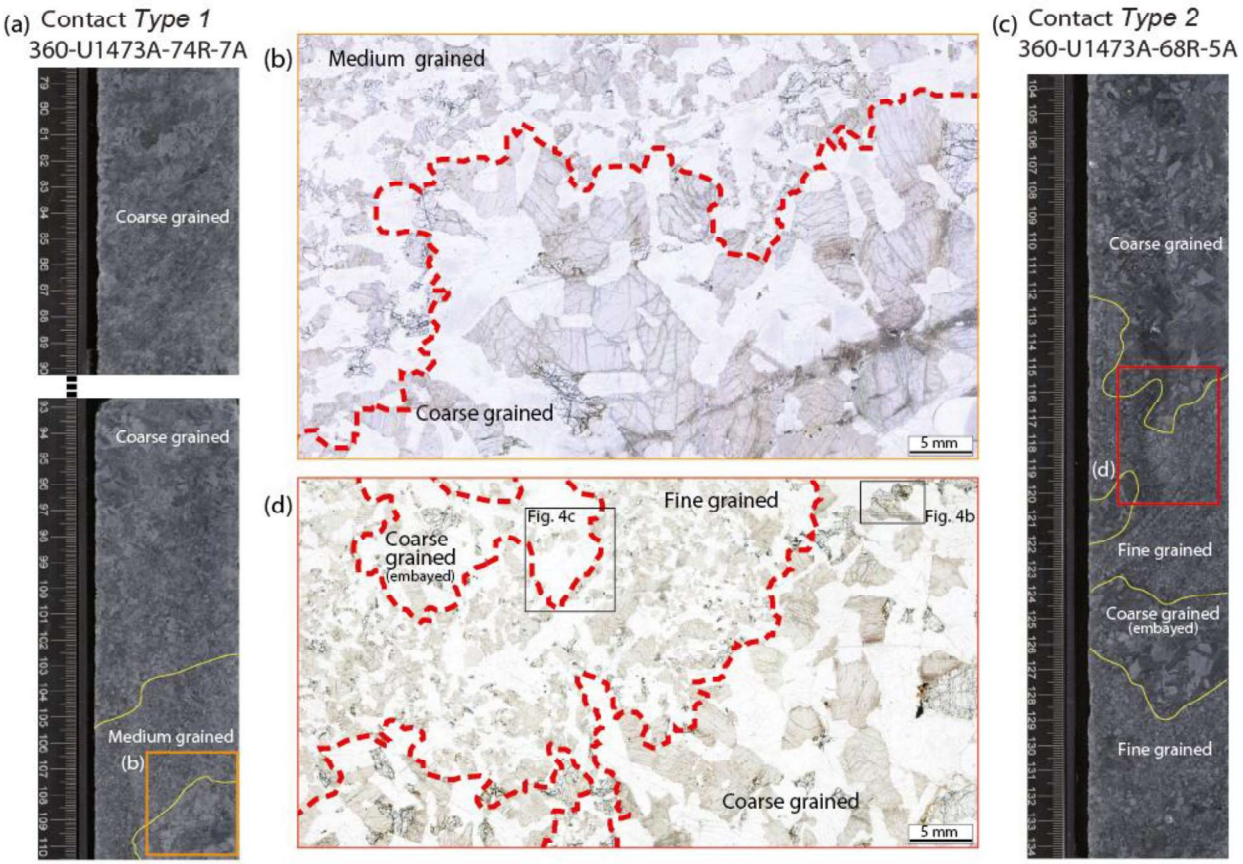

Fig. 3: Examples of (a, c) recovered irregular grain-size contacts in U1473A olivine gabbros. (a) Core 74R-7 shows wavy and lobate *Type1* contact with a close-up (orange box) in (b). (c) Core 68R-5 displays sutured and lobate *Type 2* contacts with a close-up (red box) in (d); black boxes locate close-ups of coarse-grained olivine (Fig. 4b) and plagioclase (Fig. 4c) showing lobate grain boundaries.

4.2 Magmatic textures

Olivine gabbros from IODP Hole U1473A contain cumulus assemblages of subhedral to anhedral olivine (0.2–1.5 mm in fine-grained intervals and 2-8 mm in coarse-grained intervals), euhedral and subhedral to lath-shaped plagioclase (0.2–1.5 mm in fine-grained intervals and 1.5-10 mm in coarse-grained intervals), and poikilitic to interstitial clinopyroxene (0.2–1.5 mm in fine-grained intervals and 2-15 mm in coarse-grained intervals), locally enclosing plagioclase ± olivine chadacrysts.

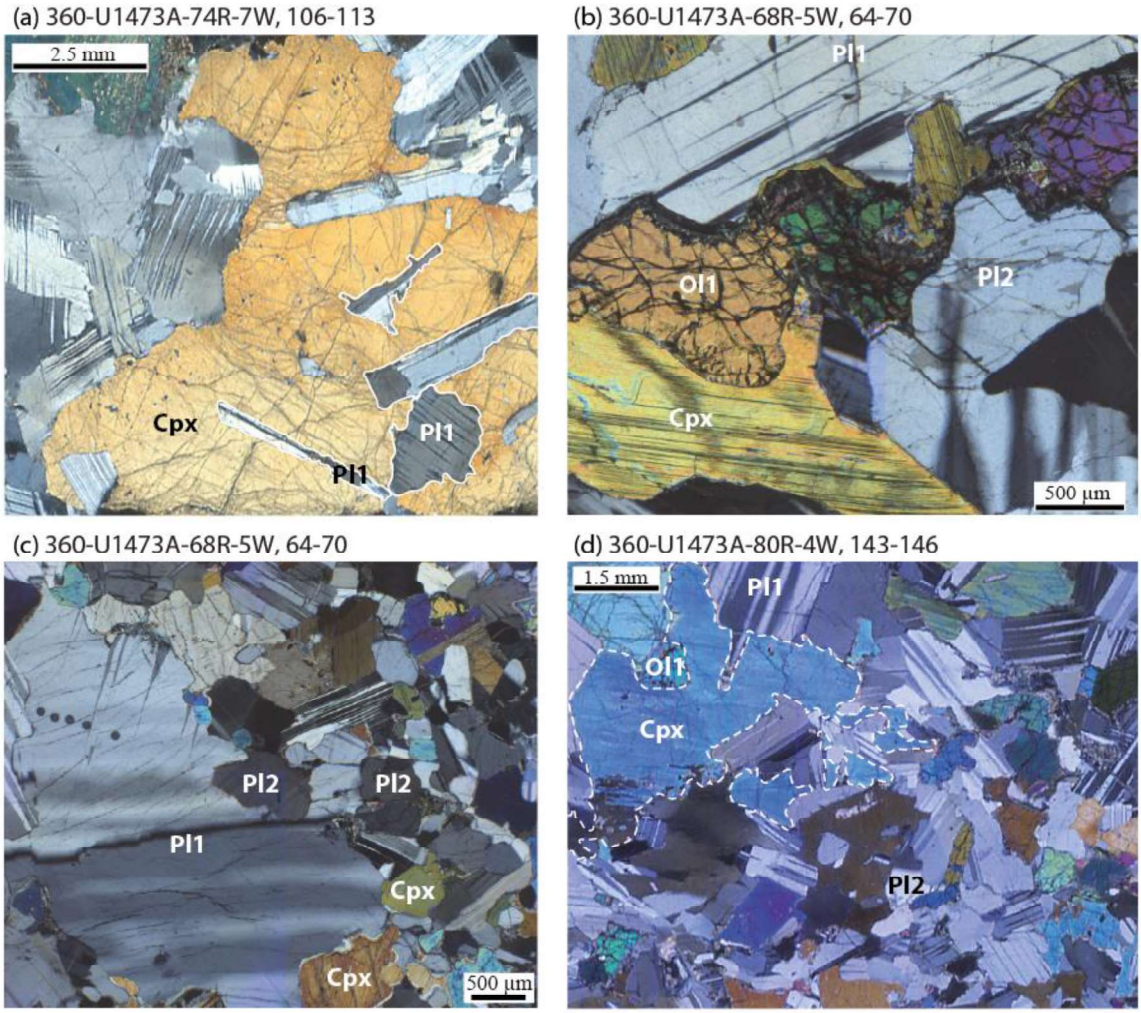

Fig. 4: Textural variability in (a-b) coarse-grained olivine gabbro and (c-d) coarse- to fine-grained olivine gabbro from IODP Hole U1473A. Name of samples are noted on top of each photomicrograph (cross polarized light). (a) Large poikilitic clinopyroxene oikocryst embay plagioclase showing corroded grain boundaries. (b) Coarse-grained plagioclase and olivine display lobate grain boundaries against interstitial and locally vermicular clinopyroxene. (c) Coarse-grained plagioclase displays corroded grain boundaries at contact with fine-grained crystals (mostly plagioclase and clinopyroxene). (d) Coarse-grained clinopyroxene at contact with fine-grained material is in optical continuity with fine grained clinopyroxene indicating that they constitute the same single crystal.

Textures of coarse-grained olivine gabbro are predominantly subophitic with subhedral tabular plagioclase partly or fully enclosed within poikilitic clinopyroxene (Fig.4a). Plagioclase chadacrysts and coarse-grained crystals display magmatic twins, and also show mechanical twins and local undulose extinction indicative of incipient crystal plastic deformation. They have lobate grain boundaries against clinopyroxene. Olivines are deformed and show kink bands. Locally, olivines display corroded contacts against adjacent interstitial clinopyroxene (Fig. 4b) and fine-grained plagioclase as well. Large oikocrysts of

clinopyroxenes show little undulose extinction, thus indicating that they are slightly deformed.

Fine-grained olivine gabbros are characterized by granular textures (Fig. 4c). Plagioclases are euhedral to subhedral (Fig. 4c,d) and are characterized by the scarce occurrence of mechanical twins (Fig. 4c). Olivines mainly appear as subhedral to anhedral undeformed crystals. Clinopyroxenes occur as subhedral crystals and locally enclose subhedral plagioclase (Fig. 4d) ± olivine; they display little undulose extinction.

At grain-size contacts, coarse-grained plagioclase displays lobate grain boundaries against fine-grained minerals (Fig. 4c). Poikilitic coarse-grained clinopyroxene can be found in optical continuity with the interstitial clinopyroxene within the fine-grained olivine gabbro (Fig. 4d), thus indicating that they are a single crystal. On the other hand, fine-grained plagioclase is never found in optical continuity with the coarse-grained counterpart and always occurs as new nuclei.

5. Mineral compositions

Representative major, minor and trace element compositions of olivine, plagioclase and clinopyroxene are reported in Supplementary Material Table S2. In the following, we present the overall mineral compositions of fine-grained and coarse-grained crystals.

5.1 Major and minor elements

Minerals from olivine gabbros in Hole U1473A have major element compositions comparable with compositions of olivine, plagioclase and clinopyroxene from ODP Hole 735B (Dick et al., 2002; Boulanger et al., 2020; Boulanger, 2020; Sanfilippo et al., 2020; Zhang et al., 2020; Figs. 5, 6).

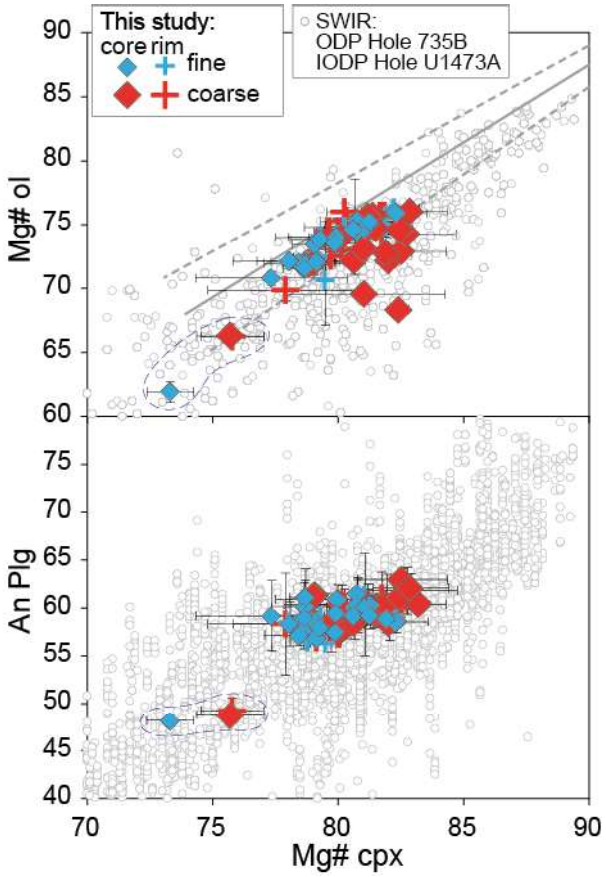

Fig. 5: Coarse- (red) and fine-grained (blue) clinopyroxene Mg# (Mg# = 100 × cationic (Mg/(Mg+Fe)) vs olivine Mg# and An content in plagioclase (average mineral composition per sample) from the studied olivine gabbros. Data are compared with theoretical Fe–Mg equilibrium between olivine and clinopyroxene, assuming mineral-melt Fe–Mg partition coefficients of 0.30 for olivine and 0.23 for clinopyroxene (Roeder and Emslie, 1970). The dashed lines represent the calculated olivine–clinopyroxene equilibrium line assuming an uncertainty of ±0.02 on the mineral–melt partition coefficients. Compositions of clinopyroxene-olivine and clinopyroxene-plagioclase in olivine gabbros from the nearby recovered ODP Hole 735B (Dick et al. 2002; Boulanger et al., 2020) and recent data from IODP Hole U1473A (Boulanger, 2020; Sanfilippo et al., 2020; Zhang et al., 2020) are reported for comparison. The dashed circles highlight the most evolved mineral compositions in sample 360-U1473A-83R-4W, 118-124 cm.

Olivine crystals show no systematic core-to-rim chemical variations. Overall, they have homogeneous compositions within single grain-size intervals, but vary with no systematic correlations throughout the Hole. Coarse-grained olivine has Mg# ranging on average from 66 to 76 mol% (average per sample in Fig. 5), low compatible elements (Ni = 375-680 ppm, Co = 180-222 ppm) and high moderately incompatible elements (Mn = 2314-3402 ppm, Zn = 84-155 ppm). Mainly across *Type 1* contacts, fine-grained olivines display slightly lower contents in compatible elements, but similar moderately incompatible elements compared to coarse-

grained olivines. All olivines display remarkably low Ca contents (Ca = 105-563 ppm), with the fine-grained olivine showing the lowest values.

Plagioclase crystals have An contents ranging on average from 56 to 64 mol% (average per sample in Fig. 5). Coarse-grained plagioclases exhibit a typical chemical zoning, marked by the decrease in An contents from the crystal cores to their rims. Fine-grained plagioclase is unzoned. Chemical heterogeneity between fine- and coarse-grained plagioclase are exclusively observed at the scale of single grain-size contacts, more specifically in Type 1 contacts. There, cores of coarse-grained plagioclase display higher An contents compared to their relative rims, which have compositions comparable to unzoned fine-grained crystals.

Clinopyroxene crystals show the most heterogeneous composition among all phases (Figs. 5, 6) with a wide compositional range of Mg# (72-86 mol%, Fig. 5), but rather comparable Cr_2O_3 contents between crystal cores and rims (Fig. 6a). Exception is made for some crystal cores displaying higher Cr_2O_3 contents compared to their relative rims (Fig. 6a). Coarse-grained clinopyroxenes display an evident chemical zoning characterized by a decrease in Mg# (79-86 mol% at crystal cores to 76-82 mol% at rims; Fig. 5), Al_2O_3 (2.93±0.70 wt% to 2.62±0.60 wt%; Fig. 6b) and Ni contents (109±19 ppm to 94±14 ppm) coupled with an increase in TiO_2 (from 0.55±0.25 wt% to 0.91±0.30 wt%; Figs. 6c, 7) from the cores to the rims of the crystals. Notably, at a given olivine Mg#, cores of coarse-grained clinopyroxene have Mg# higher than the predicted composition of clinopyroxene in equilibrium with coexisting olivine (Fig. 5). Fine-grained clinopyroxenes are chemically unzoned, and share similar compositions with rims of coarse-grained crystals (Fig. 5, 6).

Sample 360-U1473A-83R-4W, 118-124 cm displays the most evolved mineral compositions ($Mg\#_{ol}$ = 61-66 mol%, An = 48-51, $Mg\#_{cpx}$ = 72-76) among all olivine gabbros from this study (Fig. 5), testifying the local variability in mineral compositions throughout the Hole. Their in-sample chemical variability is related to the zonation of coarse-grained crystals, and to the more evolved signature of fine-grained minerals compared to the adjacent coarse-grained minerals.

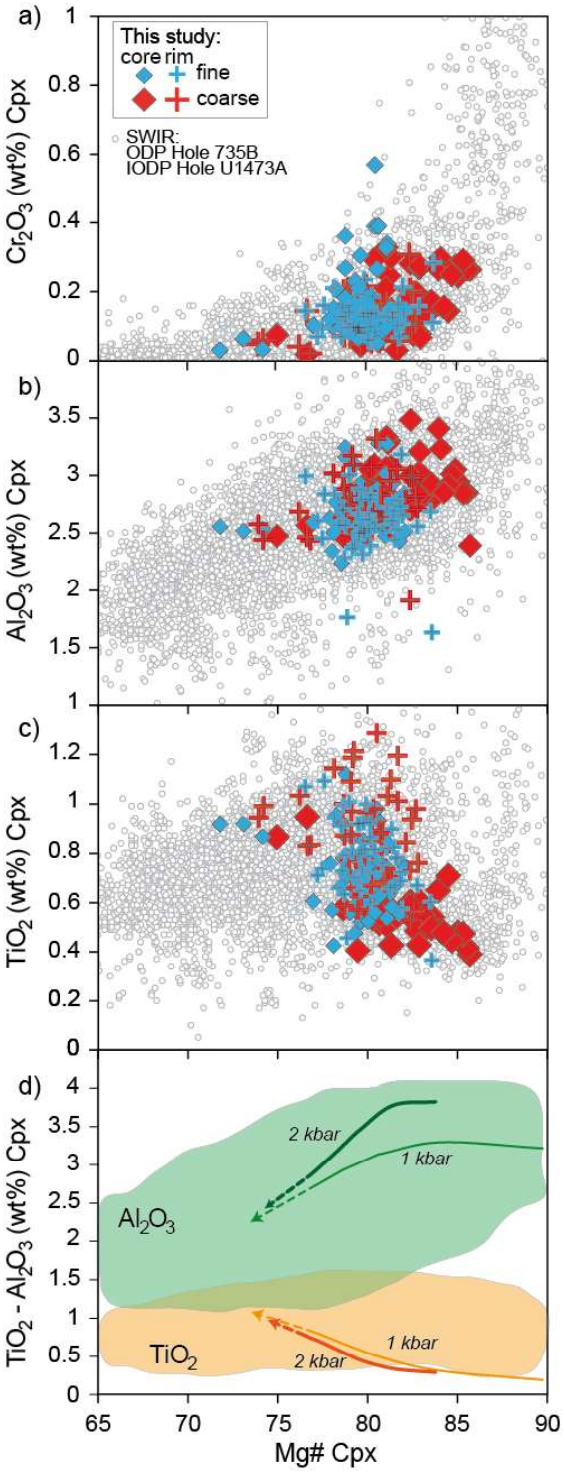

Fig. 6: Clinopyroxene major element compositions in coarse- (red) and fine-grained (blue) intervals: Mg# vs a) Cr_2O_3 (wt%), b) Al_2O_3 (wt%), and c) TiO_2 (wt%). uncertainty of ±0.02 on the mineral–melt partition coefficients. Compositions of clinopyroxenes from the nearby recovered ODP Hole 735B (Dick et al. 2002; Boulanger et al., 2020) and recent data from IODP Hole U1473A (Boulanger, 2020; Sanfilippo et al., 2020; Zhang et al., 2020) are reported for comparison. d) Al_2O_3 (wt%; in green) and TiO_2 (wt%; in orange) clinopyroxene lines of descent for crystallization at 2 kbar (dark-thick lines) and 1 kbar (light-thin lines); clinopyroxene chemical evolution is predicted by crystallization experiments of a tholeiitic basalt with the composition of a microgabbro from Hole 735B (Feig et al. 2006).

5.2 Trace elements

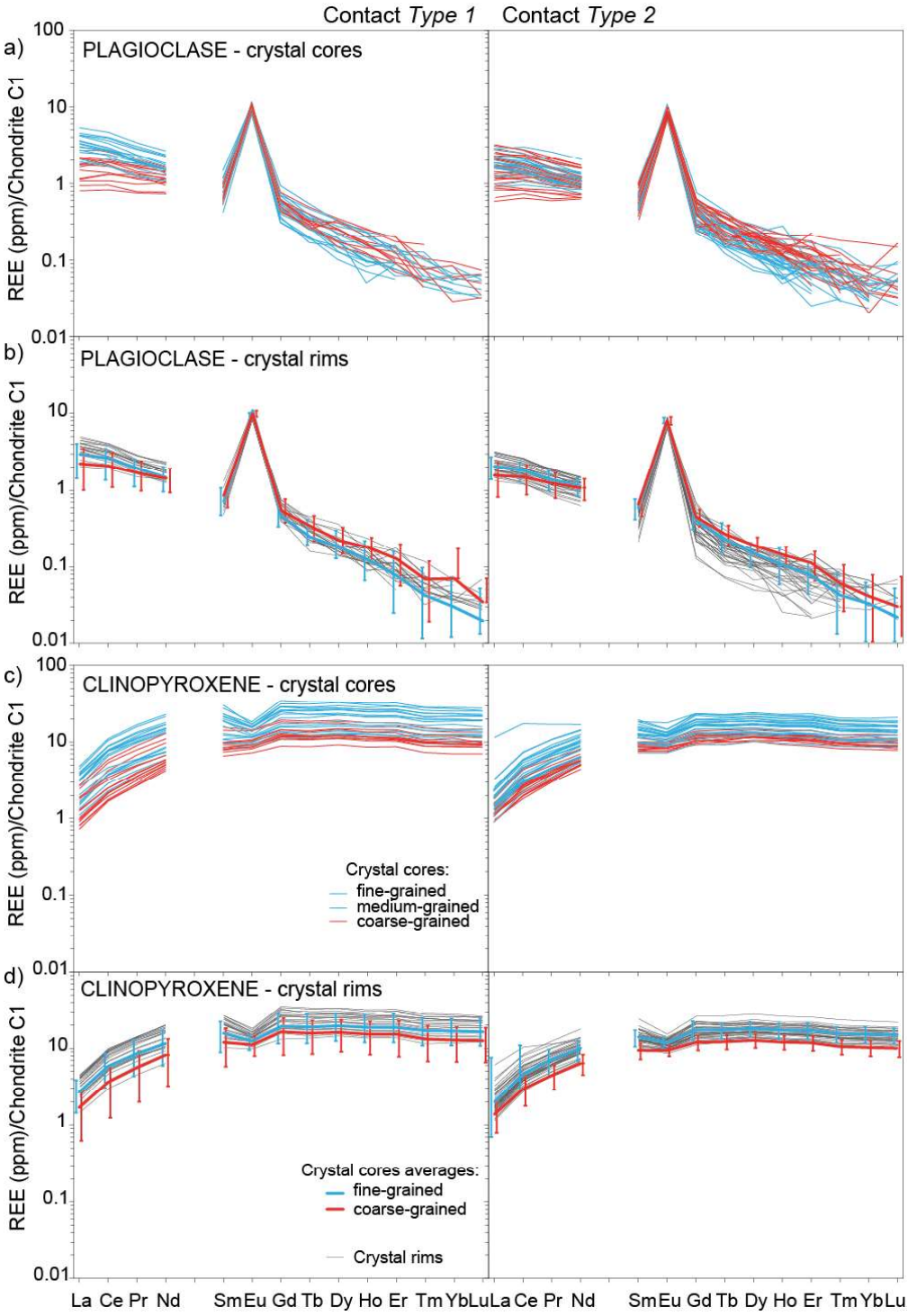

Fig. 7: Chondrite-normalized Rare Earth Element (REE) concentrations of plagioclase (a-b) and clinopyroxene (c-d) from U1473A olivine gabbros characterized by *Type 1* (left column) and *Type 2* (right column) grain-size contacts. In (a) and (c) we plot compositions of crystal cores; in (b) and (d) average compositions of crystal cores (colors refer to the size of crystals: coarse in red, and fine in blue) are compared with crystal rims (grey lines). Colored bars in (b) and (d) indicate the single-element compositional range of crystal cores. Normalizing values are after Sun and McDonough (1989).

Minerals trace element contents display different in-sample geochemical heterogeneity, i.e. *Type 1* and *Type 2* contacts can be distinguished by distinct variations in mineral compositions across the contacts. Overall, *Type 1* contacts are characterized by marked geochemical variations between coarse- and fine-grained minerals, while *Type 2* contacts display minor geochemical heterogeneity (Figs. 7, S1, S2). Here we describe the mineral trace element compositions of all analyzed phases regardless of the type of contact; the detailed discussion about geochemical heterogeneity across the two types of contacts will be given in the Discussion (section *7.3*).

Olivines are on average depleted in lithophile trace elements (Figs. S1, S2a,b in Supplementary Material). They display strong normalized H (heavy) - REE to M (medium) - REE fractionations (Dy_N/Yb_N = 0.02–0.12, Fig. S1). Olivines show strong enrichments in the most incompatible High Field Strength Elements (HFSE), such as Ti and Zr-Hf, relative to elements with similar partition coefficients during mantle melting (hereafter, referred to as 'neighboring trace elements' in spider diagrams; Fig. S2a,b). These enrichments and the HREE to MREE fractionations of the studied olivines are similar to those observed in olivines modified during melt reactive porous flow in gabbroic rocks from ophiolitic massifs (e.g., Alpine ophiolites; Sanfilippo et al., 2014; Rampone et al., 2016; Basch et al., 2018) and oceanic crustal sequences from slow-spreading oceanic centers (e.g., IODP Hole U1473A and ODP Hole 735B; Boulanger, 2020; Boulanger et al., 2020; Atlantis Massif OCC; Drouin et al., 2009; Ferrando et al., 2018). Cores of coarse-grained olivine have on average higher MREE, HREE and HFSE concentrations compared to cores of fine-grained olivine (Fig. S1, S2a). Both fine- and coarse-grained olivines are geochemically unzoned (Fig. S1, S2b), although some rims of coarse-grained olivine show lower MREE, HREE and HFSE contents than their relative cores (Fig. S1, S2b).

Plagioclases display prominent positive Eu anomalies (Eu/Eu* = 10-31; Fig. 7a,b). L (light) -REE contents (Ce_N = 0.65-4.66) vary in a range comparable with compositions of plagioclase in olivine gabbros from the Kane area (MAR, MARK area; Ce_N = 0.47-5.42; Coogan et al. 2000a,b). Trace element patterns show positive anomalies in Sr and Ti relative to neighboring elements, and negative anomalies in Zr (Fig. S2c,d). Coarse-grained plagioclases show zoning in trace elements marked by an overall increase in concentrations toward the crystal rims, which is in accord with their major element signature. Although zonation of coarse-grained plagioclases in major and trace elements recall a magmatic differentiation trend, the enrichments in trace elements cannot be reproduced by pure

fractional crystallization process (Fig. S3a). Specifically, crystal cores display nearly flat LREE patterns (Ce_N = 0.65-4.11) and rather low LREE to MREE fractionations (Ce_N/Sm_N = 1.28-3.64; Fig. 7a), whereas rims have higher LREE contents (Ce_N = 0.96-4.66) leading to stronger REE fractionations (Ce_N/Sm_N = 1.32-5.48; Fig. 7b). Fine-grained plagioclases are unzoned and show trace elements compositions similar to rims of coarse-grained plagioclase (Fig. 7b, S2c,d).

Clinopyroxenes have nearly flat patterns for MREE and HREE (Yb_N = 6.9-34.4), and variable depletion in LREE (Fig. 7c,d). Their REE contents are similar, but reach more evolved compositions compared to the composition of clinopyroxenes in olivine gabbros from the MARK area (Yb_N = 7.2-10.9; Coogan et al., 2000a,b). All clinopyroxenes are distinguished by moderate negative anomalies in Ti, while contents of Zr-Hf are significantly variable from depleted to enriched relative to neighbor trace elements (Zr_N/Nd_N = 0.42-1.85). Negative anomalies are also observed for Sr and Pb on extended trace element patterns (Fig. S2e,f). Coarse-grained clinopyroxenes display zoning in trace elements characterized by an overall increase in concentrations toward the crystal rims, which is in agreement with their major element signature. As observed in coarse-grained plagioclase, this geochemical zoning cannot be reproduced by a pure fractional crystallization process (Fig. S3b). In detail, crystal cores have low trace elements contents (Yb_N = 6.9-17.1 ppm, Fig. 7c; Zr = 7.4-40.3 ppm, Figs. S2e, S3b) and display fractionated patterns of LREE to Y (Ce_N/Y_N = 0.18-0.43) and no to little Eu negative anomalies (Eu/Eu* = 0.81-1.02). Rims of coarse-grained crystals exhibit a pronounced Eu negative anomaly (Eu/Eu* = 0.55-0.84), and enrichments in the most incompatible elements (Ce_N = 2.3-17.4, Fig. 7d; Zr = 9.8-101.1 ppm, Fig. S2f) compared to the least incompatible (Y_N = 8.1-28.4, Fig. 7d; Nd = 2.1-7.5 ppm, Fig. S2f). These trace elements concentrations are typically reported in clinopyroxene from other olivine gabbros from Hole 735B (Gao et al., 2007; Lissenberg & MacLeod, 2016) and result in increasing trace elements fractionations from the cores (Zr_N/Nd_N = 0.42-0.89; Fig. S2e) to the rims (Ce_N/Y_N = 0.23-0.87 and Zr_N/Nd_N = 0.42-1.17; Fig. S2f) of the crystals. Fine-grained clinopyroxene are overall unzoned and have compositions similar to the rims of coarse-grained clinopyroxene (Fig. 7d, S2f).

6. Equilibrium temperatures

Plagioclase-clinopyroxene and olivine-clinopyroxene equilibrium temperatures were computed to investigate temperatures of magmatic processes recorded in olivine gabbros from Hole U1473A. Temperatures were determined using two geothermometers based on partitioning of REE between the two mineral pairs considered. The geothermometer from Sun et al. (2017) was used for plagioclase-clinopyroxene pairs, while the geothermometer from Sun and Liang (2012, 2013, 2014) for olivine-clinopyroxene. Because LREE and MREE contents in olivine are close to the detection limit, and thus to avoid the analytical error, we considered only HREE and Y for calculation of the olivine-clinopyroxene equilibrium temperatures.

Equilibrium temperatures between plagioclase and clinopyroxene range in the interval 1050-1160°C (± 50°C; Fig. 8). The highest temperatures are recorded in pairs of coarse-grained crystal cores (1100-1160°C) and decrease towards fine-grained crystal cores (1060-1090°C). Equilibrium temperatures calculated using compositions of crystal rims vary in a narrower range with no systematic variations (1070-1105°C). The latter are within-error similar to temperatures measured at cores of fine-grained crystals, and thus lower than the one obtained from cores of coarse-grained crystals. Our equilibrium temperatures are comparable with temperatures estimates from olivine gabbros in the nearby ODP Hole 735B (Boulanger et al., 2020). In particular, temperature estimates from rims of coarse-grained and unzoned fine-grained clinopyroxene-plagioclase pairs overlap with equilibrium temperatures from the most evolved olivine gabbros in the lower crustal section at the Atlantis Bank OCC.

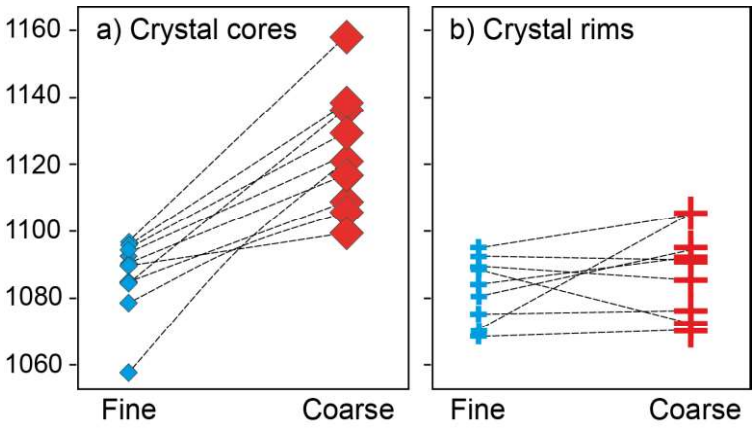

Fig. 8: Equilibrium temperatures recorded in plagioclase-clinopyroxene pairs. Temperatures were calculated between cores (a) and rims (b) of coarse- (red) and fine-grained (blue) crystals, using the geothermometer from Sun et al. (2017). Colors and symbols are as in Figures 5 and 6.

Equilibrium temperatures between olivine and clinopyroxene are overall lower than 1000°C (Fig. S4), thus suggesting chemical re-equilibration of trace element in olivine under subsolidus conditions (Sun & Liang, 2014). The lower MREE, HREE and HFSE contents at the rims of some coarse-grained olivine compared to their cores is consistent with element redistribution and diffusion from the olivine crystal to the adjacent mineral phases (mainly clinopyroxene; Sun and Liang, 2012, 2013, 2014). Also, the absence of zonation in fine-grained olivines showing on average the lowest trace element contents is in line with complete re-equilibration during cooling, which is documented to be achieved more rapidly over shorter distances (e.g., Coogan et al., 2007 and references therein). Re-equilibration at subsolidus conditions is further indicated by the very low Ca contents in the studied olivines, which point to Ca redistribution from olivine into clinopyroxene during cooling of the oceanic crustal sequence (e.g., Coogan et al., 2005, 2007; Faak & Gillis, 2016; Ferrando et al., 2020). Thus, equilibrium temperatures and the geochemical signature of olivine in the olivine gabbros from Hole U1473A indicate that the primary magmatic composition of olivine was modified during exhumation and cooling of the crustal sequence. For this reason, only plagioclase and clinopyroxene compositions are considered in the following discussion.

7. Discussion

7.1 Assessing the dominant magmatic process forming the olivine gabbro

7.1.1 A pure magmatic crystallization process?

The poikilitic textures of coarse-grained olivine gabbros are characterized by large oikocrysts of clinopyroxene embaying chadacrysts of plagioclase ± olivine (Fig. 4a). These relationships may recall primary cumulus textures resulting from the solidification of slowly cooled mafic crystal mushes (e.g., Holness et al., 2007; Nielsen et al., 2015). The studied fine-grained olivine gabbros are characterized by granular textures (Fig. 4c) likely resulting from *in-situ* adcumulus growth (e.g., O'Driscoll, 2005). Both poikilitic and granular minerals may form during pure magmatic crystallization of various magma pulses in a magmatic body, where minerals are unmodified after crystal accumulation (e.g., Holness et al., 2015). Overall, in the gabbros from the Atlantis Bank OCC (this study; Dick et al., 2002; Boulanger et al., 2020; Sanfilippo et al., 2020; Zhang et al., 2020), the decrease in clinopyroxene Mg# coupled with a decrease in olivine Mg# and An in plagioclase (Fig. 5), together with the decrease in

452 Cr_2O_3, Al_2O_3 and TiO_2 in clinopyroxene at decreasing Mg# (Fig. 6), may be reproduced at
453 first order by pure fractional crystallization at rather low pressures (Fig. 6d).

454 Although textures and mineral major element compositions suggest a common
455 crystallization process, minor and trace element compositions of minerals call for the
456 involvement of additional magmatic processes. The coarse-grained olivine gabbro selected for
457 the present study exhibits clinopyroxene and plagioclase geochemical zoning. From the core
458 to the rim of clinopyroxene, compatible elements decrease (e.g., Mg# and Cr; Figs. 5, 6), Sr
459 and Eu anomalies deepen, and incompatible elements increase (Figs. 7, S2). With respect to
460 plagioclase core, the rims are enriched in LREE, and slightly depleted in HREE and Y (Fig.
461 7). Notably, crystal rim compositions display enrichments in some of the most incompatible
462 elements, such as Zr in clinopyroxene and Ce in plagioclase (Fig. S3), thereby leading to
463 stronger fractionations of most/less incompatible elements, namely Ce_N/Y_N and Zr_N/Nd_N in
464 clinopyroxene and Ce_N/Y_N and Ce_N/Sm_N in plagioclase (Fig. S5). Ti is also remarkably
465 enriched at the rims of clinopyroxene crystals (Fig. 6c), especially at Type 1 contacts (Fig. 9).
466 These minor and trace element enrichments exceed values predicted for pure crystallization at
467 (low) pressures assumed for gabbros formation beneath slow-spreading ridges (e.g., Vanko &
468 Stakes, 1991; Kelley & Fruh-Green, 2001; Feig et al., 2006; Grimes et al., 2008; Figs. 9, S3,
469 S5).

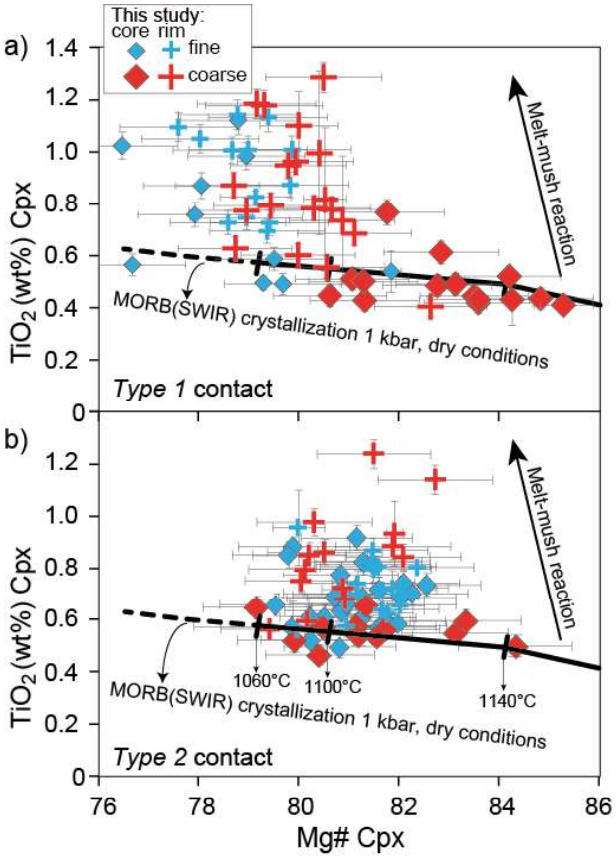

Fig. 9: Mg# vs TiO_2 (wt%) of clinopyroxene in a representative sample of *Type 1* (a) and *Type 2* (b) grain-size contacts. Notice the heterogeneous clinopyroxene compositions across *Type 1* contact (more primitive cores of coarse-grained crystals to more evolved rims and unzoned fine-grained crystals), whereas clinopyroxenes across *Type 2* contact are homogeneous. We report for comparison variations in clinopyroxene compositions during: *i)* melt-mush reaction reproduced in reactive crystallization experiments of a primitive MORB percolating through a troctolite (Yang et al. 2019); *ii)* crystallization experiments of a tholeiitic basalt with composition corresponding to a microgabbro from Hole 735B at 1 kbar (Feig et al. 2006).

Enrichments in incompatible elements at crystal rims were described in plutonic gabbroic rocks (e.g., Bédard et al., 2009), and their origin was ascribed to the entrapment of small aliquots of melt within a crystal matrix as the system cools (see also Meyer et al., 1989; Elthon et al., 1992; Bédard, 1994). To assess the potential contribution of trapped melt crystallization in selected olivine gabbros, we used the Equilibrium Distribution Method (EDM; Bédard, 1994; Bédard et al., 2009) to model the geochemical evolution of clinopyroxene during late-stage crystallization in a closed system. We considered the bulk and mineral compositions of a sample (U1473A-68R-5-W,103-110 cm) showing a marked mineral zoning (Fig. S6a,b; see figure caption for further details of the model parameters). Based on the modal composition, the proportion of crystallizing phases was set to 5% olivine, 60% plagioclase and 35% clinopyroxene, and the trapped melt fraction was assumed to vary

between 20% and 0.5%. The entrapment of low amounts of trapped melt (<2%; Fig. S6a,b) can increase both the elemental concentrations and the fractionations of most/less incompatible element ratios. However, the model is not able to reproduce the observed crystal rim compositions (Fig. S6a,b). In addition, the process of extreme melt fractionation (i.e., marked decrease in melt mass down to ~2% of the initial melt mass) leads to saturation in Fe-Ti oxide phases, orthopyroxene and amphibole (Feig et al., 2006; Koepke et al., 2018), which are not observed in the studied olivine gabbros. We conclude that fractional crystallization coupled with melt entrapment in a closed system is not the dominant process forming the Hole U1473A olivine gabbros.

In an alternative petrogenetic hypothesis, Langmuir (1989) proposed that enrichments in incompatible elements in minerals from a continental layered intrusion resulted from '*in situ* crystallization'. The latter involves crystallization at the margins of a magma chamber and return of the remaining melt fraction into the chamber interior. This process was also considered to explain the global incompatible trace element over-enrichment observed in MORBs (Coogan & O'Hara, 2015). We tested the ability of *in situ* crystallization to reproduce the trace element enrichments observed at the crystal rims in samples selected for the present study, by using the equation proposed by Langmuir (1989) (Fig. S6c-f; see figure caption for further details on the model parameters). Trends of *in situ* crystallization were simulated for different aliquots of melt returning in the magma chamber interior (f = 0.1 and 0.2; Fig. S6c-f). They predict increasing REE concentrations in the crystallizing phases as melt fractionates, and reproduce a minor range of most/less incompatible element fractionations of analyzed clinopyroxene and plagioclase grains. However, even considering the most fractionated melt returning to the magma chamber (f = 0.1) the model fails to reproduce the highest trace element fractionations observed for clinopyroxene and plagioclase (Fig. S6c-f).

In summary, magmatic crystallization, including processes of pure fractional crystallization (Figs. S3, S5) and *in situ* crystallization (Fig. S6c-f), may be considered as a plausible process forming the cores of coarse-grained minerals. However, it fails to simulate the marked over-enrichments in the most incompatible elements compared to the least incompatible elements observed for clinopyroxene-plagioclase pairs in selected coarse-grained olivine gabbros. We emphasize that a process of melt entrapment in a closed system implies a process of late-stage crystallization (F <20%; Fig. S6a-b), which is not consistent with the formation of crystal cores representing, in the case of the studied lower oceanic crustal sequence, early crystallized melt fraction (F ~80%). We conclude that another

magmatic process must be invoked, likely occurring after crystallization of primary crystal cores.

7.1.2 A reactive crystallization process producing trace element over-enrichments

The studied coarse-grained olivine gabbros display remarkable irregular shape and resorbed grain boundaries of the plagioclase chadacrysts (Fig. 4a). Locally, olivine also displays resorbed grain boundaries against interstitial to poikilitic clinopyroxene (Fig. 4b). These textural features resemble those of olivine gabbros from other sections of slow-spreading oceanic crust that locally experienced dissolution-precipitation processes, involving olivine and plagioclase dissolution by a melt that precipitated clinopyroxene (e.g., Lissenberg & Dick, 2008; Sanfilippo et al., 2015; Lissenberg & MacLeod, 2016; Boulanger et al., 2020). Chemical disequilibrium in olivine-clinopyroxene Mg# is also commonly documented in dissolution-precipitation textures, indicating olivine partial assimilation prior to clinopyroxene crystallization (e.g., Coogan et al., 2000b; Lissenberg & Dick, 2008; Drouin et al., 2009; Sanfilippo et al., 2013, 2015; Ferrando et al., 2018; Basch et al., 2019a). Consistently, the cores of coarse-grained clinopyroxenes from the studied olivine gabbros have higher Mg# (~82-84 mol%) compared to the calculated Mg# of clinopyroxene (~80-82 mol%) in equilibrium with coexisting olivine with Mg# ~72-74 mol% (Fig. 5). Interestingly, at the Atlantis Bank OCC, cryptic variations in mineral major element compositions (database reported by Dick et al., 2002) have been interpreted as re-equilibration of a crystal mush with melts percolating by permeable flow (Dick et al., 2002).

Intra-crystalline trace element zoning has been described in most gabbroic sequences (e.g., Coogan et al., 2000b; Tribuzio et al., 2000; Borghini & Rampone, 2007; Gao et al., 2007; Drouin et al., 2009; Lissenberg et al., 2013; Sanfilippo et al., 2015, 2020; Lissenberg & MacLeod, 2016; Basch et al., 2018; Ferrando et al., 2018; Boulanger et al., 2020; Zhang et al., 2020). Typically, trace element concentrations from the crystal cores to the rims are marked by a preferential increase in the most incompatible elements (Zr, Hf, LREE) compared to less incompatible elements (M-HREE, Y), as those observed in this study (see comparison in Fig. S5). Remarkable Zr_N/Nd_N positive anomalies in clinopyroxene (see Fig. S2f) have been described in gabbroic sequences as marker of mineral-melt interactions (e.g., Borghini & Rampone, 2007). Specifically for gabbros from the Atlantis Bank OCC, several authors have suggested that these mineral zoning can result from assimilation of the pre-existing gabbroic

minerals and concomitant crystallization of new phases (i.e., assimilation-fractional crystallization, AFC) during reactive porous flow (Gao et al., 2007; Lissenberg & MacLeod, 2016; Boulanger et al., 2020; Sanfilippo et al., 2020; Zhang et al., 2020). Yet, we have shown that enrichments in Ti as those observed at the rims of analyzed clinopyroxenes cannot be reproduced by simple magmatic differentiation (i.e., fractional crystallization; Fig. 9). These Ti enrichments were recently reproduced experimentally after reactive percolation of a primitive MORB in a troctolitic crystal-matrix (Yang et al., 2019). Likewise, the zoning of coarse-grained minerals in the studied olivine gabbros possibly formed after a process of mineral-melt interactions. The peculiar geochemical zoning have been successfully reproduced using the AFC equations proposed by DePaolo (1981) (e.g., Lissenberg et al., 2013; Sanfilippo et al., 2015; Lissenberg & MacLeod, 2016; Boulanger et al., 2020; Sanfilippo et al., 2020; Zhang et al., 2020). We thus also performed AFC modelling to test whether a process of reactive crystallization is able to reproduce the ubiquitous over-enrichments in the most incompatible trace elements (i.e., LREE and Zr) observed in the studied olivine gabbros.

The occurrence of large poikilitic clinopyroxene suggests that the percolated matrix was a crystal mush with more than ~30 vol% occupied by melt between the crystal framework (e.g., Coogan et al., 2000b). Because no evidence of dissolution was observed at clinopyroxene grain boundaries, we assume that clinopyroxene was minor or nearly absent in the initial mush; on the other hand, olivine and plagioclase show resorbed grain boundaries. We thus posit that the crystal mush was mainly composed of olivine (ol_1) + plagioclase (pl_1) and minor clinopyroxene; during the process of melt reactive porous flow, the crystal matrix was partially dissolved and olivine (ol_2) + plagioclase (pl_2) + clinopyroxene (cpx_2) crystallized. Mineral modal compositions of the starting ol_1 + pl_1 crystal mush were determined using MELTS (Ghiorso & Sack, 1995) after 20 % of fractional crystallization of a primitive N-MORB from the studied area (Mg# ~62; Coogan et al., 2004). This threshold of melt fractionation was chosen to reproduce a troctolitic matrix containing <5 vol% of clinopyroxene. These computed mineral modes were used to calculate the trace element compositions of the assimilated crystals (ol_1 + pl_1); the latter were determined using the common equation of fractional crystallization after 20% of melt fractionation (ol_1 and pl_1 in equilibrium with $C_{20\%F} = C_0*(F^{(Gk-1)})$, where C_0 is the composition of the initial melt, i.e. the primitive N-MORB with Yb_N ~15.6; F is the melt fraction; Gk is the global partition coefficient of a given element, determined using the partition coefficients calculated from our

588 mineral compositions using models by Sun & Liang, 2014 and Sun et al., 2017). The
589 composition of the migrating melt was estimated from the composition of cores of coarse-
590 grained clinopyroxene. Major and trace element compositions of coarse-grained crystal cores
591 are in equilibrium with a N-MORB compositionally similar to the primitive end-members
592 among MORBs from the SWIR (Mg# ~62 mol%; Coogan et al., 2004). The calculated melt
593 (in equilibrium with average core of coarse-grained clinopyroxene) has on average Mg# ~62
594 mol% and low trace element contents (Yb_N ~17.3; Fig. S7). Conversely, rims of coarse-
595 grained clinopyroxene and unzoned fine-grained crystals crystallized from a more evolved
596 melt that, calculated in equilibrium with an average of the fine-grained crystals, has Mg# ~53
597 mol% and higher trace element contents (average evolved MORB from the SWIR: Yb_N =
598 25.2; Coogan et al., 2004; Fig. S7).

599 The mineral-melt interaction process described above was modelled assuming the
600 following reaction (AFC-1):

601 $0.4\ ol_1 + 0.6\ pl_1 + melt_1 = 0.1\ ol_2 + 0.6\ pl_2 + 0.3\ cpx_2 + melt_2$

602 where ol_1 (olivine) and pl_1 (plagioclase) constitute the pre-existing crystal matrix (Ma -
603 assimilated mass), $melt_1$ is the migrating melt before reactive crystallization, and ol_2 + pl_2 +
604 cpx_2 (clinopyroxene) are the minerals in equilibrium with the reacted and modified $melt_2$ and
605 constituting the olivine gabbro (Mc - crystallized mass). The mineral modes of the products
606 are representative of the modal compositions of the studied olivine gabbros.

607 The results of the AFC-1 modelling are reported in Figure 10a,b in terms of Yb_N vs
608 Zr_N/Nd_N in clinopyroxene and Sm_N vs Ce_N/Sm_N in plagioclase. Computed AFC-1 trends (Fig.
609 10a,b) show the compositions of clinopyroxene and plagioclase in equilibrium with the
610 modified melt during the reactive process ($melt_2$) at progressively decreasing melt mass (F =
611 0.95–0.05). We set five different Ma/Mc (Ma/Mc = 0.6-0.8) representing different extents of
612 the reactive process. These AFC-1 models succeed in reproducing most of the increase in
613 REE of clinopyroxene and plagioclase (i.e., Yb and Sm, respectively) in olivine gabbros from
614 Hole U1473A. They simulate the lower interval of trace element fractionations, which
615 increase progressively during the reaction and characterize a portion of analyzed fine-grained
616 minerals. Note, however, that our AFC-1 fails to reproduce the most enriched Zr
617 concentrations at rims of coarse-grained clinopyroxene and some fine-grained
618 clinopyroxenes. In the following, we hypothesize a further step of the AFC process to explain
619 the most extreme trace element enrichments.

620

621

622

623

624

625

626

627 **Fig. 10**: Variation of Zr_N/Nd_N ratio vs Yb_N in clinopyroxene (a, c, e) and Ce_N/Sm_N ratio vs Sm_N in
628 plagioclase (b, d, f) of coarse- (dark grey) and fine-grained (light grey) olivine gabbro from this study.
629 Symbols are as in Figures 5, 6 and 8. Data are compared to clinopyroxene and plagioclase composition
630 computed by AFC models (De Paolo, 1981) at decreasing melt mass and using different Ma/Mc ratios.
631 Partition coefficients were calculated at 1100°C from mineral compositions measured in this study
632 using the lattice-strain model from Sun and Liang (2014) for olivine and clinopyroxene, and Sun et al.
633 (2017) for plagioclase. a-b) Results of AFC-1 models that reproduce olivine + plagioclase assimilation
634 and crystallization of olivine gabbro; first step of the model is computed at F = 1 (100% melt mass).
635 The initial melt composition ($melt_1$; yellow star) is equal to the melt computed in equilibrium with the
636 average REE composition of clinopyroxene cores in the more primitive U1473A coarse-grained
637 olivine gabbros. Note that this model does not explain the most over-enrichments in Zr in
638 clinopyroxene. c-f) Results of AFC-2 models that reproduce assimilation of olivine gabbro from AFC-
639 1 models and crystallization of gabbro. The initial melt and mineral compositions ($melt_2$) are: (c-d)
640 output of AFC-1 run at Ma/Mc = 0.65 after F = 0.55 (white star; AFC-2a), first step of AFC-2a model
641 is assumed to correspond to 55% melt mass; (e-f) output of AFC-1 run at Ma/Mc = 0.8 after F = 0.20
642 (blue star; AFC-2b), first step of AFC-2b model is assumed to correspond to 20% melt mass.

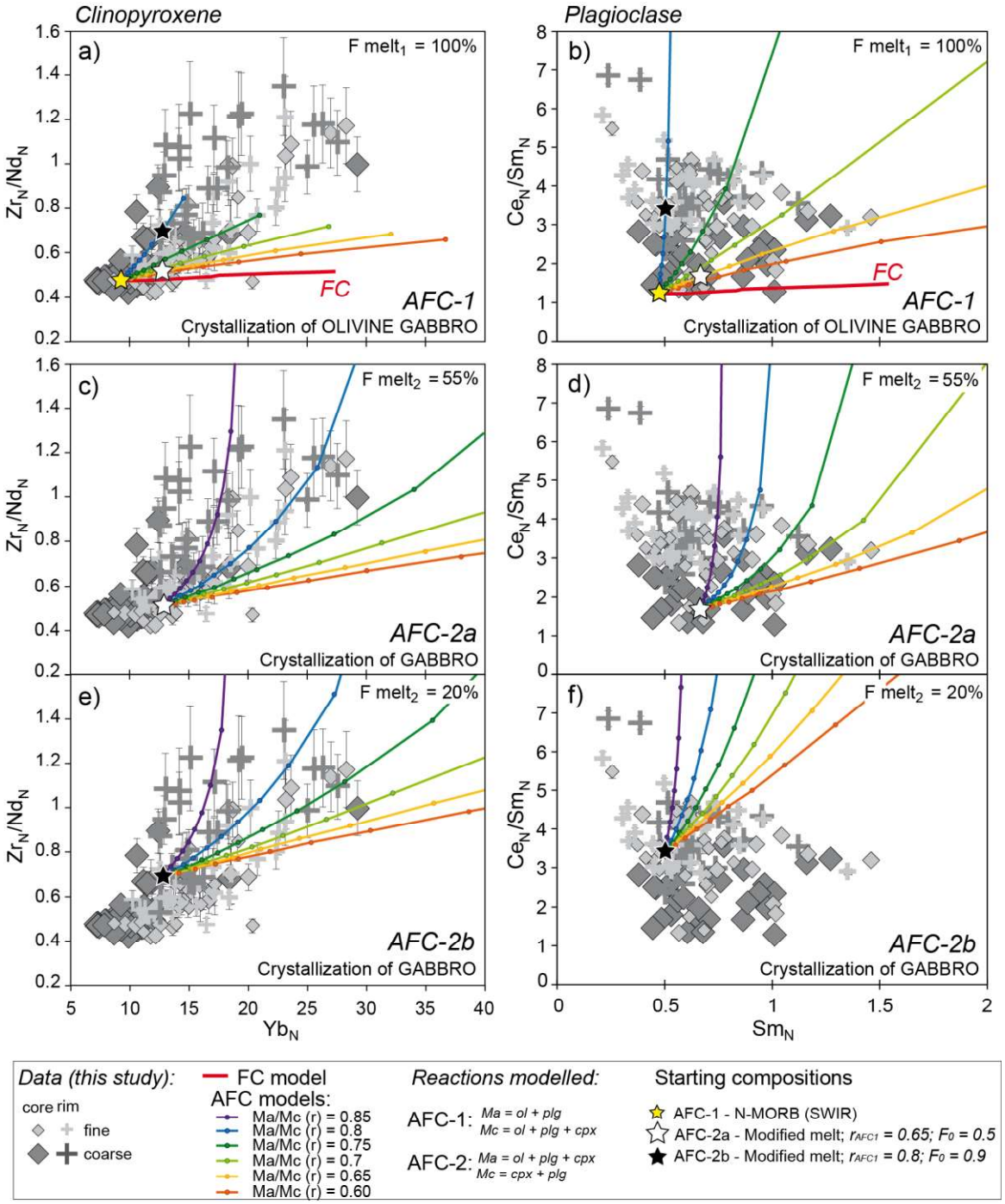
Clinopyroxene
Plagioclase
a)
b)
c)
d)
e)
f)
F melt1 = 100%
F melt2 = 55%
F melt2 = 20%
FC
AFC-1
AFC-2a
AFC-2b
Crystallization of OLIVINE GABBRO
Crystallization of GABBRO
ZrN/NdN
CeN/SmN
YbN
SmN
Data (this study):
core rim
fine
coarse
FC model
AFC models:
Ma/Mc (r) = 0.85
Ma/Mc (r) = 0.8
Ma/Mc (r) = 0.75
Ma/Mc (r) = 0.7
Ma/Mc (r) = 0.65
Ma/Mc (r) = 0.60
Reactions modelled:
AFC-1: Ma = ol + plg
Mc = ol + plg + cpx
AFC-2: Ma = ol + plg + cpx
Mc = cpx + plg
Starting compositions
AFC-1 - N-MORB (SWIR)
AFC-2a - Modified melt; rAFC1 = 0.65; F0 = 0.5
AFC-2b - Modified melt; rAFC1 = 0.8; F0 = 0.9

643

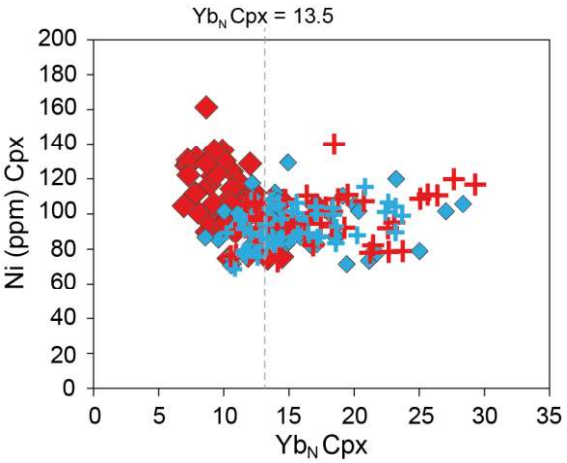

Fig. 11: Ni (ppm) vs Yb_N in clinopyroxene. At Yb_N < ~13.5 Ni decrease at increasing Yb_N; at > ~13.5 Ni is nearly constant at increasing Yb_N. Symbols are as in Figures 5 and 6.

The strong trace element fractionations observed at rims of coarse-grained and in some fine-grained clinopyroxene (i.e., not explained by AFC-1; Fig. 10a) are coupled with constant Ni at increasing REE (Fig. 11), thus suggesting that Ni does not vary in the parental melt as crystallization proceeds. This contrasts with the composition of cores of coarse-grained crystals that show decreasing Ni during mineral-melt interactions and progressive crystallization (i.e., at increasing REE; Fig. 11). Because Ni partitioning is significantly higher in olivine than in clinopyroxene ($^{ol/melt}Kd_{Ni} \approx 10$ and $^{cpx/melt}Kd_{Ni} \approx 3.8$; Le Roux et al., 2011), variations of Ni contents in clinopyroxene can be used to trace the crystallization of olivine (see also Sanfilippo et al., 2015). Concomitant crystallization of olivine and clinopyroxene leads to decreasing Ni in the parental melts as magmatic crystallization proceeds (Fig. 11). When olivine crystallization ceases, Ni becomes only weakly compatible to incompatible, as it is governed by the crystallization of plagioclase and clinopyroxene only. Furthermore, experimental studies and thermodynamic evaluations suggest that during melt crystallization and AFC processes, the melt residual from interactions may differentiate following a liquid-line of descent different from that expected by a fractional crystallization process (Kvassnes & Grove, 2008; Collier & Kelemen, 2010; Basch et al., 2019a). Here, we propose that at temperatures ~1050°C (roughly corresponding to the rims of coarse-grained minerals and to the fine-grained intervals) the melt is no longer saturated in olivine and the crystallizing assemblage is mainly constituted by plagioclase and clinopyroxene (e.g., Feig et al., 2006; Husen et al., 2016). This is demonstrated by the constant Ni contents in the rims of the coarse-grained clinopyroxene as well as in the fine-grained counterparts, which likely crystallized from a residual melt undersaturated in olivine. To test this hypothesis, we

669 performed AFC models to reproduce the geochemical evolution of clinopyroxene and
670 plagioclase during the reaction (AFC-2):

671 $ol_2 + plg_2 + cpx_2 + melt_2 = plg_3 + cpx_3 + melt_3$

672 where $ol_2 + plg_2 + cpx_2$ constitute the olivine gabbro formed during AFC-1, $plg_3 + cpx_3$ are
673 crystal rims of plagioclase and clinopyroxene, respectively, precipitated from the reacted
674 $melt_3$. We considered the variation in Ni vs Yb_N contents in clinopyroxene to constrain the
675 change in olivine saturation in the melt, and thus to pinpoint the melt composition at which
676 olivine ceased to crystallize. At increasing Yb_N, Ni in clinopyroxene decreases until $Yb_N \sim$
677 13.5, after which it remains relatively constant (Fig. 11). The melt in equilibrium with this
678 clinopyroxene has Yb_N = 23.5-23.8. We selected this melt composition and the corresponding
679 bulk-rock composition from the output of AFC-1. Two starting compositions were chosen
680 along trends of AFC-1 models run at two distinct Ma/Mc ratios (Fig. 10c-f), by selecting
681 $melt_2$ with $Yb_N \sim$ 23.5-23.8:

682 *(i) AFC-2a* uses bulk rock and melt compositions from AFC-1 run with Ma/Mc = 0.65; $melt_2$
683 with Yb_N =23.5-23.8 was reproduced after 45% crystallization of N-MORB during AFC-1;

684 *(ii) AFC-2b* uses bulk rock and melt compositions from AFC-1 run with Ma/Mc = 0.8; $melt_2$
685 with Yb_N =23.5-23.8 was reproduced after 80% crystallization of N-MORB during AFC-1.

686 The results of the AFC-2 models are reported in Figure 10c,d,e,f. The compositions of
687 plagioclase and clinopyroxene rims are successfully reproduced by AFC-2 at a relatively high
688 Ma/Mc (up to Ma/Mc = 0.85) and considering less than 80% crystallized melt mass. The
689 deepening of the Eu negative anomaly in clinopyroxene from the crystal cores to the rims
690 further indicate the decrease in melt mass during the late stages of the reactive process. Thus,
691 such evolved compositions record the closure of the system and final melt crystallization,
692 which likely occurred at decreasing temperature and porosity of the crystal mush.

693 We would like to stress that mineral trace element compositions across single grain-size
694 contacts generally lay along the same reaction curve corresponding to a given Ma/Mc of the
695 AFC-1 models (Fig. S8). Ma and Mc are function of the rate of assimilation and
696 crystallization, respectively (DePaolo, 1981). The AFC process is thus strongly dependent
697 upon the disequilibrium between the melt and the crystals, which controls the rate of
698 assimilation, and the conditions favoring melt crystallization (i.e., controlling the rate of
699 crystallization). Assuming a constant rate of crystallization, for instance governed by a

constant heat removal from the lower oceanic crust (e.g., Coogan et al., 2007), the variable Ma/Mc in the studied olivine gabbros could be related to local variations in melt-mineral chemical disequilibrium. It is possible that locally different melt composition or variations in mineral compositions throughout the crystal mush could enhance or reduce the rate of assimilation.

In conclusion, we here demonstrated that olivine gabbros from IODP Hole U1473A form during two dominant magmatic processes; they involve early crystallization of a gabbroic matrix in a crystal mush, and subsequent mineral-melt reactions driven by melt reactive porous flow.

7.2 Origin of coarse- vs fine-grained crystals

We have shown that the studied samples display variations in grain size and have relatively homogeneous mineral modal compositions. The higher crystal density per volume within the fine-grained olivine gabbros compared to the coarse-grained intervals (Fig. 3), suggests that nucleation was more efficient during crystallization of the fine-grained crystals. Conversely, crystal growth was the dominant crystallization mechanism during formation of coarse-grained minerals (see Mollo & Hammer, 2017, and references therein). Crystals nucleation and growth are strongly controlled by the difference between liquidus temperature (T_L) and effective temperature of the crystallizing melt (i.e., temperature of the system, T_S), namely the degree of undercooling (e.g., Donaldson, 1976; Kirkpatrick et al., 1976; Dowty, 1980; Faure et al., 2003; O'Driscoll et al., 2007; Martel, 2012; Mollo & Hammer, 2017; Barbey et al., 2019; Mourey & Shea, 2019; Shea et al., 2019). When T_S is close to T_L (i.e., low degrees of undercooling), and for example when a primitive MORB crystallizes in-situ in a rather hot system (~1200°C), crystal growth predominates. At rather constant T_L, the undercooling can only increase with the decrease of T_S (see Mollo & Hammer, 2017, and references therein). When T_S starts to decrease (e.g., injection in a relatively cool host rock), and therefore at slightly higher degrees of undercooling, new nuclei start to form and crystallization is dominated by nucleation (Lofgren, 1980). Significant and abrupt perturbations in T_L (e.g., Donaldson, 1977; Hammer & Rutherford, 2002; O'Driscoll et al., 2007; Welsch et al., 2013; Barbey et al., 2019; Basch et al., 2019a) can also markedly change the degree of undercooling and leads to disequilibrium growth textures (e.g., Donaldson, 1974; Faure et al., 2007), even at small degrees of undercooling (25-40°; Shea et al., 2019).

At the Atlantis Bank OCC, we showed that a progressive chemical evolution is recorded from the cores of coarse-grained crystals to their respective rims, the latter sharing the same compositions with the fine-grained minerals; therefore, T_L and T_S are progressively modified upon magmatic differentiation with no abrupt change in both T_L and T_S. Accordingly, the fine-grained intervals are characterized by granular textures of mostly polyhedral crystals (Donaldson, 1974; Faure et al., 2007).

The progressive chemical evolution recorded in coarse-grained minerals resulted from reactive porous flow (see section *7.1.2*). Thermal models indicate that decrease in T_S is expected to accompany a process of chemical equilibration of the melt with the mineral matrix during the process of reactive melt migration in crystal mushes (Solano et al., 2014). This idea is sustained by Sanfilippo et al. (2020) who documented thermal equilibration towards lower T during a process of reactive migration into a melt-rich channel crosscutting an olivine gabbro from Hole U1473A. Following these findings, we suggest that the formation of coarse-grained intervals is thereby characterized by a progressive decrease in T_S, associated with a progressive decrease in T_L due to the change in melt composition during reactive porous flow. This hampered the development of an undercooling, and crystal growth dominated.

The equilibrium temperatures recorded in cores of coarse-grained mineral phases (~1150°C; Fig. 8a) are ~100°C higher than those measured in fine-grained intervals (~1050°C; Fig. 8a). Rim-rim equilibrium temperatures both in coarse- and fine-grained intervals are comparable to the fine-grained core-core equilibrium temperatures (Fig. 8b). This is consistent with the similar compositions of rims of coarse-grained minerals and unzoned fine-grained minerals, thereby indicating that they crystallized from melts having the same composition and T_L. Despite these chemical similarities, textural evidence i.e., growth of rim of coarse-grained crystals vs nucleation of fine-grained minerals, indicate a change in crystallization mechanism due to the presence or absence of pre-existing nuclei. While coarse-grained minerals continuously grew at decreasing T_L and T_S, the same evolved melt was collected in melt-rich intervals with no pre-existing nuclei, thus possibly preventing crystal growth. This likely led to a delay in nucleation in those melt-rich domains (e.g., Koepke et al., 2011; Mollo & Hammer, 2017 and references therein) that allowed the T_L to remain constant during the progressive cooling of the system (i.e., decrease in T_S). This generated significant undercooling in those areas, and in turn enhanced crystals nucleation rate, leading to the formation of the fine-grained olivine-gabbro.

765 To summarize, we infer that coarse-grained intervals formed during melt reactive
766 percolation in a crystal mush at temperatures T_S close to the T_L of the melts (i.e., low
767 undercooling). These conditions favored the growth of pre-existing minerals associated with
768 low nucleation rates (e.g., Martel, 2012). Upon cooling, and likely due to melt segregation, a
769 delay in nucleation created a significant undercooling, in turn resulting in the crystallization
770 of melt-rich intervals dominated by crystal nucleation. Simultaneously, in the coarse-grained
771 intervals, the interstitial melts, compositionally similar to fine-grained minerals, precipitated
772 at the crystal rims due to the presence of pre-existing nuclei, and have the most evolved
773 compositions. We emphasize that the equilibrium temperatures recorded in the fine-grained
774 intervals likely do not represent the temperature of melt segregation, but rather are minimum
775 estimates of the crystallization temperature of the adcumulate fine-grained olivine gabbros
776 (i.e., when olivine, plagioclase and clinopyroxene crystallized simultaneously). Nonetheless,
777 the 100°C difference between coarse- and fine-grained intervals represents the primary
778 difference in crystallization temperature.

779

780 **7.3 Reconstructing the temporal evolution of grain-size variations**

781 **7.3.1 Two distinct grain-size contacts**

782 Minor compositional variations are observed between coarse- and fine-grained minerals
783 across planar contacts defining an igneous layering in Hole U1473A (Boulanger, 2020; Fig.
784 12). Conversely, minerals across irregular contacts from this study display different within-
785 sample chemical heterogeneity. In particular, *Type 1* and *Type 2* irregular contacts can be
786 distinguished by distinct variations in mineral compositions across the contacts (Fig. 12).
787 Based on structural relationships and mineral geochemical compositions, we identified the
788 two types of contacts as follows.

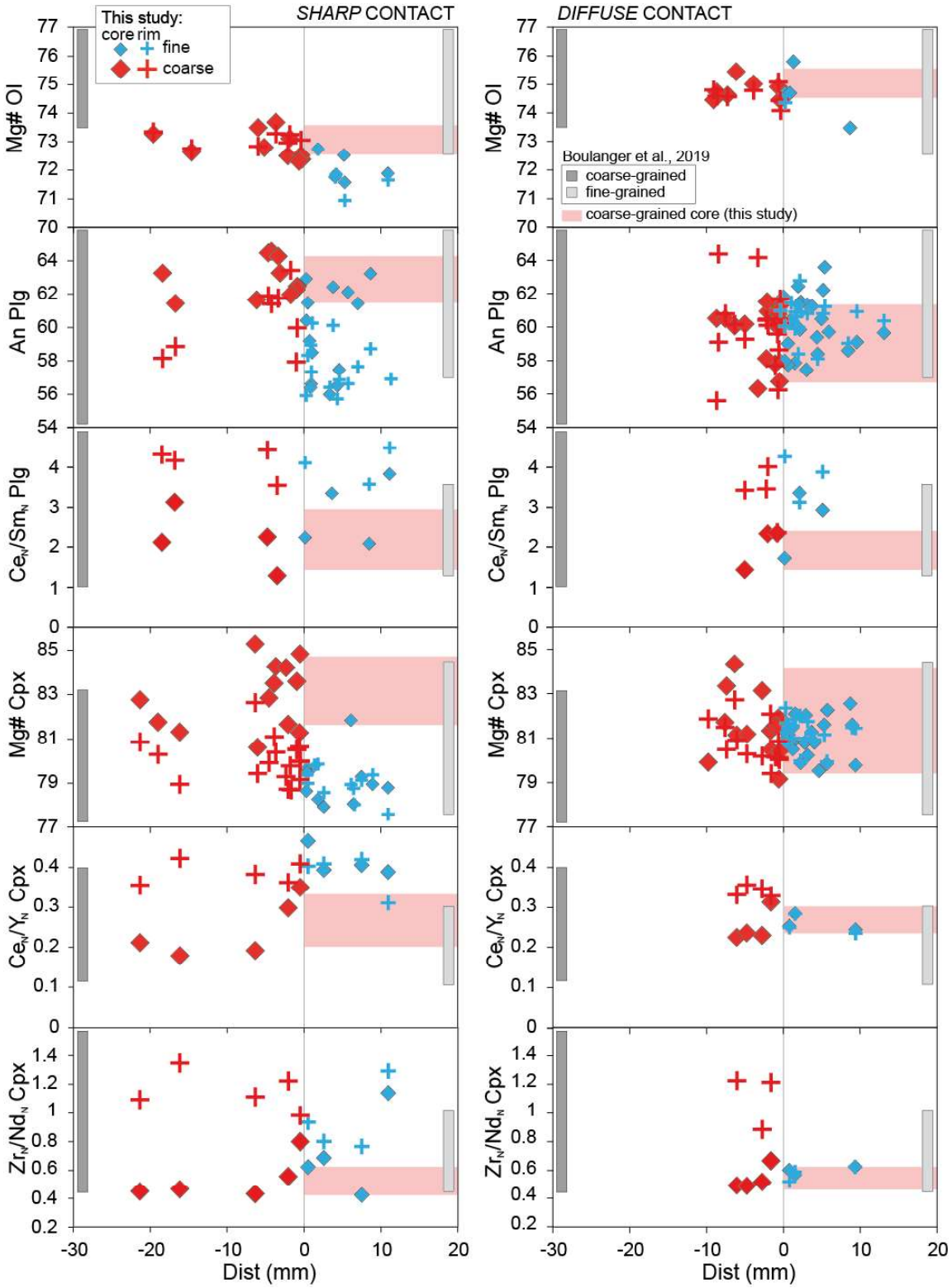

Fig. 12: Profiles of mineral (Ol = olivine, Plg = plagioclase, Cpx = clinopyroxene) chemical compositions across grain-size contacts where coarse-grained crystals are plotted on the left and fine-grained on the right of the contact (placed at 0). Two representative samples are selected: one for sharp contacts (left column; sample 360-U1473A-73R-1W, 41-47 cm) and one for diffuse contacts (right column; sample 360-U1473A-68R-5W, 64-70 cm). Red boxes are compositions of cores of coarse-grained crystals. Grey bars indicate compositional variability of coarse- (dark) and fine-grained (light) minerals in layering within olivine gabbro from the same Hole U1473A (Boulanger, 2020).

Sharp grain-size contacts show preserved thick intervals of coarse-grained olivine gabbro (*Type 1*; Fig. 3a). The mineral compositional variations between coarse- and fine-grained intervals are notable. For any given coarse-grained domain, rims of plagioclase and clinopyroxene are systematically more evolved than relative crystal cores. The crystal rims and the nearly unzoned fine-grained crystals show similar compositions (Fig. 12). This is for instance shown by the covariations in increasing Ti with decreasing Mg# in clinopyroxene (Fig. 9a), and by the progressive over-enrichments in highly incompatible elements (Ce_N/Sm_N in plagioclase; Ce_N/Y_N and Zr_N/Nd_N in clinopyroxene).

Diffuse grain-size contacts display coarse-grained olivine gabbro occurring in few cm-thick levels, locally embayed within the fine-grained intervals (*Type 2*; Fig. 3c). Overall, they display homogeneous compositions of coarse- to fine-grained minerals (Figs. 9b, 12), although REE contents of fine-grained clinopyroxene cores are slightly higher than the coarse-grained counterparts (Fig. 7c, S2e). Over-enrichments in the most incompatible elements are preferentially observed at rims of coarse-grained clinopyroxene.

Selected olivine gabbros not only record melt migration and melt chemical evolution in a reactive porous flow process (see section *7.1.2*), but also document for the first time the segregation of melts modified by this reactive process (see section *7.2*). Variations in mineral chemical compositions are systematic between coarse and fine-grained crystals across *sharp irregular* contacts (Fig. 12), whereas *diffuse irregular* contacts show rather homogeneous mineral chemistry (Fig. 12), with the clinopyroxene exception recording incompatible element differences (Figs. 7c,d, S2e,f). We infer that distinct mechanisms of reactive crystallization control mineral compositions across the two types of irregular contacts in olivine gabbros. Based on numerical simulations of melt flow in crystal mushes, Hersum et al. (2005) proposed that melt flow is markedly dependent on melt fraction: melt migration is diffuse between crystals at high melt fractions, and becomes focused with decreasing melt fraction. At *sharp* contacts, fine-grained olivine gabbros are dm-thick discrete intervals indicating focused melt migration, as similarly described in the Oman Ophiolite (e.g., Korenaga and Kelemen, 1997, 1998). This testifies melt migration at relatively low melt fractions in the selected fine-grained intervals presenting *sharp* contacts. In contrast, the ~m-thick fine-grained intervals characterized by *diffuse* contacts possibly document pervasive melt migration at high melt/rock ratio (Collier & Kelemen, 2010; Van den Bleeken et al., 2011; Saper & Liang, 2014).

Throughout Hole U1473A, the difference in melt fraction between *sharp* and *diffuse* contacts might be related to the heterogeneous distribution of crystals in the crystal mush, in turn leading to heterogeneous crystal/melt ratios. This heterogeneity may be enhanced by local variations in the strength of compaction of the crystal pile. In this scenario, higher crystal/melt ratios (i.e., lower melt fraction) allow melts to migrate at higher flow rates increasing the degree of channelization (Bergantz et al., 2015). The reacted melts migrate by focused flow, and as temperature decreases, they segregate in discrete intervals to form the fine-grained olivine gabbro. Coarse-grained intervals are preserved, and minerals retain their primary chemical composition (i.e., composition of crystal cores) as observed across *sharp* contacts in this study. Conversely, melt migration occurs interstitially between coarse-grained crystals in zones with originally lower crystal/melt ratios (i.e., high melt fraction). There, high fractions of reacted melt completely reset the chemical composition of enclosed coarse-grained phases and crystallize the fine-grained olivine gabbro, thus originating the described *diffuse* contacts.

7.3.2 From melt migration to melt segregation throughout the lower oceanic crust

Geophysical data indicate that at early stages of formation, the magmatic bodies building the oceanic crust likely contain melt with sparse crystals (Sinha et al., 1997; Singh et al., 2006). When the interstitial melts are mobilized, the buoyant melt migration and related melt-mineral interactions lead to upward chemical differentiation trends recorded in the crystallized phases (see Lissenberg et al., 2019; Boulanger et al., 2020, and references therein). Textures and mineral geochemical compositions coupled with AFC models indicate that also in Hole U1473A interstitial melts were mobilized and reacted with the pre-existing crystal mush (Fig. 13).

The composition of cores of coarse-grained minerals, partly reproduced by magmatic crystallization, together with reactive textures of olivine and plagioclase, indicate that they constitute the early crystallized phases in the crystal mush ($ol_1 + pl_1 \pm cpx_1$; Fig. 13a). Due to faster diffusion in olivine compared to plagioclase (e.g., Cherniak, 2003, 2010; Dohmen et al., 2007; Van Orman et al., 2014), olivine in the crystal mush is rapidly re-equilibrated with the reactive migrating melts by element diffusion, whereas cores of coarse-grained plagioclase typically preserve their primary composition. In interval 570-750 mbsf of IODP Hole U1473A, downhole An variations in cores of coarse-grained plagioclase are limited (58-62

mol%), with no systematic evolution trend (Fig. 14a). We infer that these compositions represent the primary composition of plagioclase prior to melt-mineral interactions and indicate a relatively homogeneous composition of the pristine crystal mush (Figs. 13a and 14b: Step1). In contrast, within the same depth interval, bulk-rock Mg# (mainly defined by olivine gabbros; Fig. 2, 14c), and Mg# and Cr contents in cores of coarse-grained clinopyroxene decrease upwards (Fig. 14c,d). Because clinopyroxene is considered in this study as a product of the AFC process, we relate this upward chemical evolution to the differentiation of melts migrating to shallower depths (see also Lissenberg et al., 2019; Fig. 14b: Step2) during reactive porous flow (Fig. 13b). Based on the thickness of the interval in which clinopyroxene and bulk compositions evolve upward, melt migration and reaction most likely occurred within an individual magmatic unit of ~200 m thickness (Fig. 14c,d); such a thickness is also consistent with the reservoir size identified at ODP Hole 735B drilled in Atlantis Bank (Boulanger et al., 2020).

Fig. 13: Schematic reconstruction of the microstructure and chemical evolution from crystal mush to formation of grain-size variations in the studied olivine gabbro. The processes recorded can be summarized as follows. (a) Heterogeneously distributed olivine + plagioclase crystals form after crystallization in-situ (up to 20-30% of melt fractionation) of primitive melts in a crystal mush. (b) Melts within the crystal mush (possibly residual from former minerals crystallization) begin to migrate through the permeable olivine+plagioclase (±clinopyroxene?) framework and, being in disequilibrium with the more primitive compositions of pre-existing minerals, partially dissolve olivine$_1$ and plagioclase$_1$ and concomitantly crystallize olivine$_2$, plagioclase$_2$ and clinopyroxene$_2$; crystals preferentially grow and coarse-grained intervals are formed at temperatures of ~1150°C. Note that only plagioclase and olivine display resorbed grain boundaries, while clinopyroxene does not show textural evidences of dissolution. It is possible that few crystals of clinopyroxene$_1$ also formed the pre-existing crystal mush; some crystal cores could represent former clinopyroxene, but we have no certain and clear evidence at this point. (c) The reactive melt migration proceeds at decreasing T_L and T_S. Melts residual from interaction both crystallize at the rims of pre-existing coarse-grained minerals and are pervasively collected in high porosity zones. In these zones, the delay in nucleation produces an increase in undercooling at decreasing T_S that ultimately results in high nucleation rates; new nuclei preferentially form, and the segregated residual melts crystallize to form the fine-grained olivine gabbros at temperatures of ~1050°C.

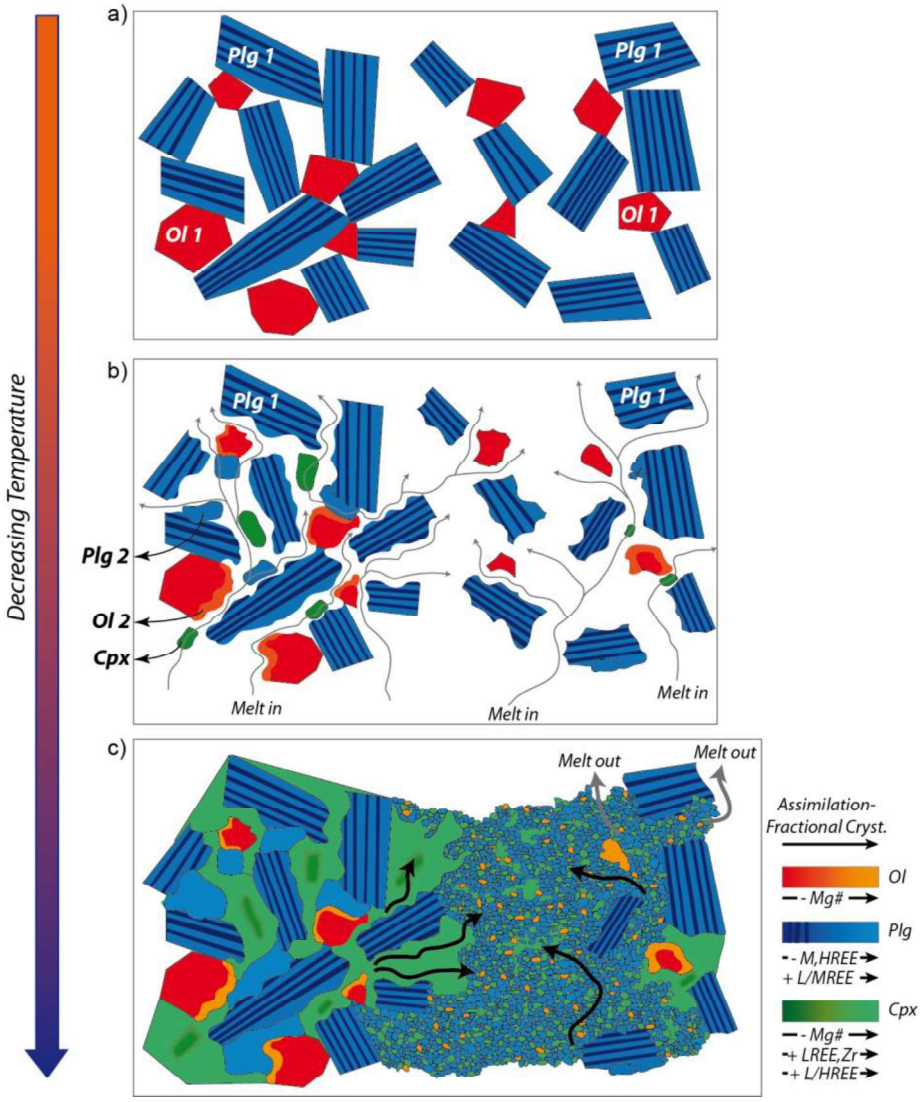

897

898 The rims of coarse-grained crystals and the unzoned fine-grained minerals crystallized
899 from genetically related parental melts (see section *7.1.2*). The latter correspond to melts
900 modified by the mineral-melt interactions in the coarse-grained crystal mush. The formation
901 of fine-grained olivine gabbros, involving enhanced crystal nucleation and hampered crystal
902 growth, required the collection and accumulation of residual melts within discrete intervals
903 where crystal nuclei were nearly absent (Fig. 13b,c). This promoted a delay in nucleation,
904 thereby increasing the degree of undercooling (see section *7.2*). The melt-rich intervals likely
905 represented zones of high porosity within the crystal mush. When the system cooled, these
906 residual melts remained segregated and crystallization was progressively dominated by
907 nucleation (i.e., at enhanced undercooling), thereby leading to the formation of the
908 adcumulate fine-grained olivine gabbros (Fig. 13c).

909 The ubiquitous textural and geochemical evidence of melt-mush interactions (mainly in
910 coarse-grained intervals) and the occurrence of the fine-grained olivine gabbros throughout

Hole U1473A indicate that reactive melt migration affected large portions of lower crust crystal mush, and that residual melts were collected and ultimately segregated at all depths in the lower oceanic crust at the Atlantis Bank OCC (Fig. 14e: Step 3). This implies that the initial stages of melt migration through the coarse-grained crystal-mush occurred interstitially between pre-existing crystals, and produced the geochemical evolution trends within a single chemical unit by pervasive melt transport (Fig. 14b,c,d - Step 2). The melts residual from the reactive processes accumulate in discrete levels where melt transport was driven by two main mechanisms. *Diffuse* contacts testify pervasive melt migration, while *sharp* contacts record focused melt migration. Both pervasive and focused melt transport occurred locally, at the scale of single fine-grained intervals (less than a meter) and governed the composition of microgabbros. The equal and homogeneous distribution with depth of the two types of contacts indicate that no predominant mechanism drove local melt transport. The local character of melt collection implies that the accumulated melts originated in the associated coarse-grained olivine gabbros as evidenced by systematically more evolved compositions of microgabbros respect to their coarse-grained counterpart; therefore, the primary chemical trend produced by early porous flow in the coarse-grained crystal mush (Fig. 14a,c and Fig. 14b: Step 2) was not affected by the diffuse and focused melt transport and accumulation (Fig. 14e: Step 3). Because bulk-rock analyses of fine-grained intervals show a cumulitic character (L. France, unpublished data), it is plausible that accumulated melts were further extracted from the melt-rich pockets (microgabbros), chemically contributing to MORBs.

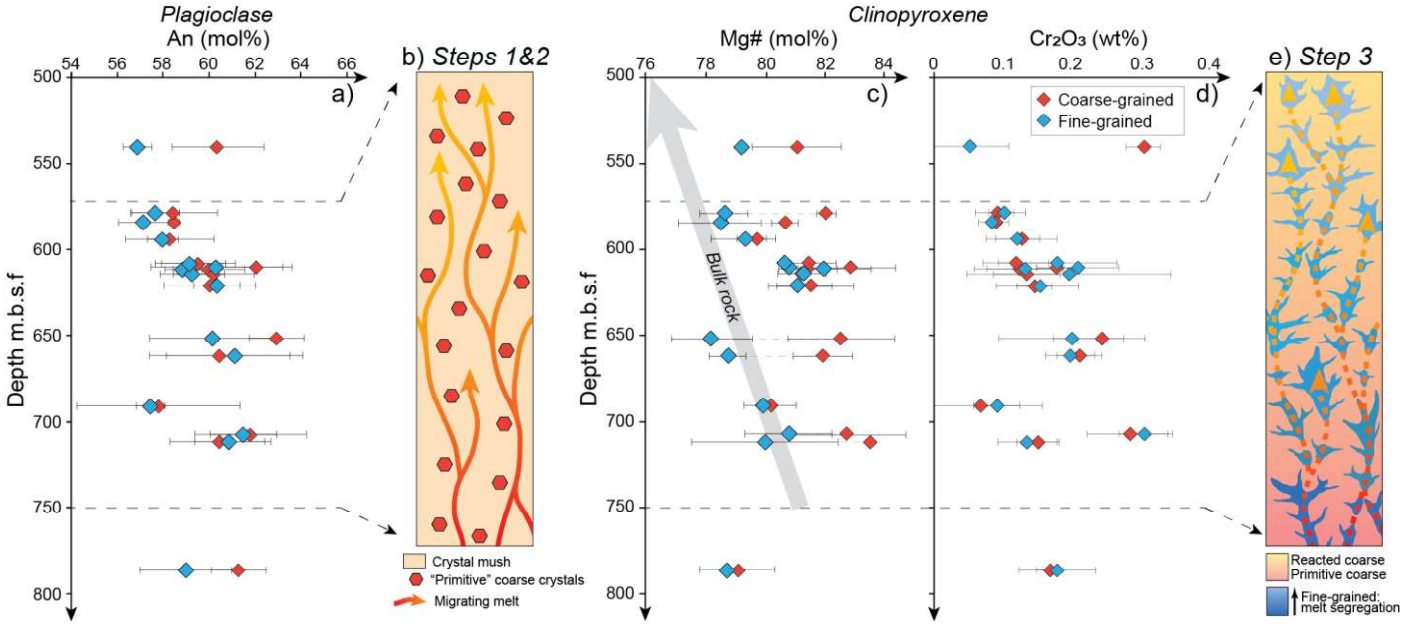

Fig. 14: Downhole An contents in plagioclase cores (a) and Mg# (c) and Cr_2O_3 (wt%; d) in clinopyroxene cores in olivine gabbro from this study, in the depth interval 500-810 mbsf. Data are averages of coarse- and fine-grained minerals from each studied sample; the grey arrow in Mg# plot (c) shows the upward chemical trend of bulk-rock compositions of olivine gabbro from Hole U1473A in the studied depth interval (MacLeod et al. 2017). Rather homogeneous compositions of coarse-grained plagioclase possibly represent components of the former crystal mush (b; Step 1) percolated by reactive melts (b; Step 2). Upward evolution of bulk and clinopyroxene compositions likely testifies the progressive differentiation of migrating melts. Such melts are ultimately segregated at all depths and form the fine-grained olivine gabbro.

9. Concluding remarks

Textures and mineral geochemical compositions coupled with AFC models are consistent with formation of U1473A olivine gabbros from ubiquitous processes of reactive porous flow of melts through a pre-existing crystal mush, which concomitantly led to upward chemical differentiation of these migrating melts. We document that the complex history of crystal mush emplacement and mineral-melt interactions at the Atlantis Bank OCC are mainly recorded in coarse-grained intervals. Fine-grained olivine gabbros testify collection and segregation of the melts residual from the reactive process, governed by cooling of the lower oceanic crust (from ~1150° to ~1050°C). The cooling could result from two processes. The first implies initiation of the detachment fault responsible for the exhumation of the lower oceanic crust at OCCs; thereby, uplifting of gabbroic sequences has been reported as efficient mechanism of heat removal (e.g.; Coogan et al., 2007; Ferrando et al., 2020) At the Atlantis Bank OCC, the average cooling rates of ~0.005 °C/yr (John et al., 2004; Coogan et al., 2007)

could be responsible for the decrease in the temperature of the system (T_S). It is plausible that exhumation was associated with reduced melt income, which further diminuished the heat supply to the lower oceanic crust and thus enhanced cooling. The second potential process triggering the cooling of the forming lower oceanic crust is the melt evolution by AFC, which is documented to be endothermic (e.g., Kelemen, 1990; Solano et al., 2014).

Geochemical compositions of erupted MORBs from different locations record melt-mineral interactions occurring in the lower oceanic crust (e.g., Lissenberg & Dick, 2008; Lissenberg et al., 2013; Boulanger et al., 2020). Our study of grain-size variations throughout IODP Hole U1473A allows identifying for the first time the collection and accumulation of melts residual from the reactive process in high-porosity zones, throughout the lower oceanic crust. Both at *diffuse* and *sharp grain-size* contacts, we propose that these accumulated melts can be at some point extracted from the lower oceanic crust and, therefore, can chemically contribute to the erupted MORBs.

Acknowledgments

The geochemical data used in this study are included as tables in the supporting information. The data published will be contributed to the Petrological Database (www.earthchem.org/petdb). The authors are grateful to an anonymous reviewer and Greg Hirth for constructive reviews, and to F. Faure for constructive discussions. We express our warm thanks to the Captain and shipboard crew of IODP Expedition 360 for their assistance in data collection at sea, and we gratefully acknowledge the Scientific Party of IODP Expedition 360 for fruitful discussions during the cruise and post-cruise meeting. We are thankful to Christophe Nevado and Doriane Delmas for providing high-quality thin sections. The authors thank B. Boyer and O. Bruguier for assistance on analytical instruments from the Microsonde Sud (Géosciences Montpellier, University of Montpellier) and AETE-ISO platform ("Analyses des Eléments en Trace dans l'Environnement et ISOtopes"; OREME observatory, University of Montpellier) respectively. This research used samples and data provided by the Integrated Ocean Discovery Program (IODP). This project was supported by CNRS-INSU through the program TelluS-SYSTER, by IODP-France funding provided to L. France and C. Ferrando, and by the Italian Ministry of Education, University and Research (MIUR) through the grant 'ECORD-IODP Italia 2018' provided to C. Ferrando. This is CRPG contribution number XXXX.

989

990 # References

991 Abily, B., & Ceuleneer, G. (2013) The dunitic mantle-crust transition zone in the Oman
992 ophiolite: residue of melt-rock interaction, cumulates from high-MgO melts, or both? *Geology*
993 41, 67–70. . https://doi.org/10.1130/G33351.1.

994 Baines, A.G, Cheadle, M.J., John, B.E., & Schwartz, J.J. (2008) The rate of oceanic
995 detachment faulting at Atlantis Bank, SW Indian Ridge. *Earth and Planetary Science Letters*,
996 273, 105–114. https://doi.org/10.1016/j.epsl.2008.06.013.

997 Barbey, P., Faure, F., Paquette, J., Pistre, K., Delangle, C., & Gremilliet, J.-P. (2019)
998 Skeletal quartz and dendritic biotite: Witnesses of primary disequilibrium growth textures in
999 an alkali-feldspar granite. *Lithos* 348–349, 105202.
1000 https://doi.org/10.1016/j.lithos.2019.105202.

1001 Basch, V., Rampone, E., Crispini, L., Ferrando, C., Ildefonse, B., & Godard, M. (2018)
1002 From mantle peridotites to hybrid troctolites: Textural and chemical evolution during melt-
1003 rock interaction history. *Lithos* 323, 4–23. https://doi.org/10.1016/j.lithos.2018.02.025.

1004 Basch, V., Rampone, E., Crispini, L., Ferrando, C., Ildefonse, B., & Godard, M; (2019a)
1005 Multi-stage reactive formation of troctolites in Slow-spreading Oceanic Lithosphere (Erro –
1006 Tobbio, Italy): a combined field and petrochemical study. *Journal of Petrology*, 60(5), 873-
1007 906. https://doi.org/10.1093/petrology/egz019.

1008 Basch, V., Rampone, E., Borghini, G., Ferrando, C., & Zanetti, A. (2019b) Origin of
1009 pyroxenites in the oceanic mantle and their implications on the reactive percolation of
1010 depleted melts. *Contribution to Mineralogy and Petrology*, 174, 97.
1011 https://doi.org/10.1007/s00410-019-1640-0.

1012 Bédard, J.H. (1994) A procedure for calculating the equilibrium distribution of trace
1013 elements among the minerals of cumulate rocks, and the concentration of trace elements in the
1014 coexisting liquids. *Chemical Geology*, 118, 143-153. https://doi.org/10.1016/0009-
1015 2541(94)90173-2.

1016 Bédard, J.H., Hebert, R., Berclaz, A., & Varfalvy, V. (2000) Syntexis and the genesis of
1017 lower oceanic crust. In: Ophiolites and oceanic crust: new insights from field studies and the

Ocean Drilling Program, Dilek, Y., Moores, E.M., Elthon, D., Nicolas, A. (Eds), *Special Paper of the Geological Society of America,* 349, 105–119. https://doi.org/10.1130/0-8137-2349-3.105.

Bédard, J.H., Leclerc, F., Harris, L.B, & Goulet, N. (2009) Intra-sill magmatic evolution in the Cummings Complex, Abitibi greenstone belt: Tholeiitic to calc-alkaline magmatism recorded in an Archaean subvolcanic conduit system. *Lithos*, 111, 47–71. https://doi.org/10.1016/j.lithos.2009.03.013.

Bergantz, G.W., Schleicher, J.M., & Burgisser, A. (2015) Open-system dynamics and mixing in magma mushes. *Nature Geosciences* 8,10. https://doi.org/10.1038/ngeo2534.

Blackman, D.K., Ildefonse, B., John, B.E., Ohara, Y., Miller, D.J., MacLeod, C.J., & the Expedition 304/305 Scientists (2006). Proceedings of the Integrated Ocean Drilling Program, vol. 304/305, *Integrated Ocean Drill Program* Manage Int, College Station, Tex. https://doi.org/10.2204/iodp.sp.304305.2004.

Blackman, D.K., Ildefonse, B., John, B.E., Ohara, Y., Miller, D.J., Abe, N., Abratis, M., Andal, E.S., Andreani, M., Awaji, S., Beard, J.S., Brunelli, D., Charney, A.B., Christie, D.M., Collins, J., Delacour, A.G., Delius, H., Drouin, M., Einaudi, F., Escartín, J., Frost, B.R., Früh-Green, G., Fryer, P.B., Gee, J.S., Godard, M., Grimes, C.B., Halfpenny, A., Hansen, H.E., Harris, A.C., Tamura, A., Hayman, N.W., Hellebrand, E., Hirose, T., Hirth, J.G., Ishimaru, S., Johnson, K.T.M., Karner, G.D., Linek, M., MacLeod, C.J., Maeda, J., Mason, O.U., McCaig, A.M., Michibayashi, K., Morris, A., Nakagawa, T., Nozaka, T., Rosner, M., Searle, R.C., Suhr, G., Tominaga, M., Von Der Handt, A., Yamasaki, T. & Zhao, X., (2011). Drilling constraints on lithospheric accretion and evolution at Atlantis Massif, Mid-Atlantic Ridge 30°N. *Journal of Geophysical Research: Solid Earth*, 116, 1–25. https://doi.org/10.1029/2010JB007931.

Borghini, G., & Rampone, E. (2007) Postcumulus processes in oceanic-type olivine-rich cumulates: The role of trapped melt crystallization versus melt/rock interaction. *Contribution to Mineralogy and Petrology,* 154, 619–633. https://doi.org/10.1007/s00410-007-0217-5.

Boulanger, M. (2020) The fate of melts within the slow-spreading lower oceanic crust: New insights from Atlantis Bank (Southwest Indian Ridge). Earth Sciences. *Ph.D. Thesis at Université de Lorraine.*

Boulanger, M., France, L., Deans, J.R., Ferrando, C., Lissenberg, J., & von der Handt, A. (2020) Magma reservoir formation and evolution at a slow-spreading center (Atlantis Bank, Southwest Indian Ridge). *Frontiers in Earth Sciences.* https://doi.org/10.3389/feart.2020.554598

Canales, J.P., Nedimovic, M.R., Kent, G.M., Carbotte, S.M., & Detrick, R.S. (2009) Seismic reflection images of a near-axis melt sill within the lower crust at the Juan de Fuca ridge. *Nature*, 460, 89-94. https://doi.org/10.1038/nature08095.

Cannat, M., Sauter, D., Mendel, V., Ruellan, E., Okino, K., Escartin, J., Combier, V., & Baala, M. (2006) Modes of seafloor generation at a melt-poor ultraslow-spreading ridge. *Geology* 34, 605–608. https://doi.org/10.1130/G22486.1.

Cashman, K.V., Sparks, R.S.J., & Blundy, J.D. (2017) Vertically extensive and unstable magmatic systems: a unified view of igneous processes. *Science,* 355, 6331. https://doi.org/10.1126/science.aag3055.

Cherniak, D.J. (2010) REE diffusion in olivine. *American Mineralogist*, 95, 362–368. https://doi.org/10.2138/am.2010.3345.

Cherniak, D.J. (2003) REE diffusion in feldspar. *Chemical Geology*, 193, 25–41. https://doi.org/10.1016/S0009-2541(02)00246-2.

Collier, J.S., & Singh, S.C. (1998) A seismic inversion study of the axial magma chamber reflector beneath the East Pacific Rise near 10°N. *Geological Society, London, Special Publications*, 148, 17–28. https://doi.org/10.1144/GSL.SP.1998.148.01.02.

Collier, M.L., & Kelemen, P.B. (2010) The case for reactive crystallization at mid-ocean ridges. *Journal of Petrology,* 51, 1913–1940. https://doi.org/10.1093/petrology/egq043.

Coogan, L.A., Hain, A., Stahl, S., & Chakraborty, S. (2005) Experimental determination of the diffusion coefficient for calcium in olivine between 900°C and 1500°C. *Geochimica et Cosmochimica Acta*, 69, 3683–3694. https://doi.org/10.1016/j.gca.2005.03.002.

Coogan, L.A., Jenkin, G.R.T., & Wilson, R.N. (2007) Contrasting cooling rates in the lower oceanic crust at fast- and slow-spreading ridges revealed by geospeedometry. *Journal of Petrology*, 48, 2211–2231. https://doi.org/10.1093/petrology/egm057.

Coogan, L.A., Kempton, P.D., Saunders, A.D., & Norry, M.J. (2000a) Melt aggregation within the crust beneath the Mid-Atlantic Ridge: evidence from plagioclase and clinopyroxene major and trace element compositions. *Earth and Planetary Science Letters*, 176, 245–257.

Coogan, L. A., & O'Hara, M. J. (2015) MORB differentiation: In situ crystallization in replenished-tapped magma chambers. *Geochimica et Cosmochimica Acta,* 158, 147–161. https://doi.org/10.1016/j.gca.2015.03.010.

Coogan, L.A., Saunders, A.D., Kempton, P.D., & Norry, M.J. (2000b) Evidence from oceanic gabbros for porous melt migration within a crystal mush beneath the Mid-Atlantic Ridge. *Geochemistry, Geophysics, Geosystems*, 1(9). https://doi.org/10.1029/2000GC000072.

Coogan, L.A., Thompson, G.M., MacLeod, C.J., Dick, H.J.B., Edwards, S., Hosford Scheirer, A., & Barry, T. (2004) A combined basalt and peridotite perspective on 14 million years of melt generation at the Atlantis Bank segment of the Southwest Indian Ridge: evidence for temporal changes in mantle dynamics? *Chemical Geology*, 207, 13–30. https://doi.org/10.1016/j.chemgeo.2004.01.016.

DePaolo, D.J. (1981) Trace element and isotopic effects of combined wallrock assimilation and fractional crystallization. *Earth and Planetary Science Letters,* 53, 189–202. https://doi.org/10.1016/0012-821X(81)90153-9.

Dick, H.J.B., Lissenberg, J., Warren, J.M. (2010) Mantle melting, melt transport, and delivery beneath a slow-spreading ridge: The paleo-MAR from 23°15°N to 23°45°N. *Journal of Petrology*, 51, 425–467. https://doi.org/10.1093/petrology/egp088.

Dick, H.J.B., Lin, J., & Schouten, H. (2003) An ultraslow-spreading class of ocean ridge. *Nature*, 426, 405–412. https://doi.org/10.1038/nature02128.

Dick, H.J.B., MacLeod, C.J., Blum, P., Abe, N., Blackman, D.K., Bowles, J.A., Cheadle, M.J., Cho, K., Ciazela, J., Deans, J.R., Edgcomb, V.P., Ferrando, C., France, L., Ghosh, B., Ildefonse, B., John, B., Kendrick, M.A., Koepke, J., Leong, J.A.M., Liu, C., Ma, Q., Morishita, T., Morris, A., Natland, J.H., Nozaka, T., Pluemper, O., Sanfilippo, A., Sylvan, J.B., Tivey, M.A., Tribuzio, R., & Viegas, G. (2019) Dynamic accretion beneath a slow-spreading ridge segment: IODP Hole 1473A and the Atlantis Bank Oceanic Core Complex.

Journal of Geophysical Research: Solid Earth, 124, 2631– 12659. https://doi.org/10.1029/2018JB016858.

Dick, H.J.B., Meyer, P.S., Bloomer, S., Kirby, S., Stakes, D., & Mawer, C. (1991a) Lithostratigraphic evolution of an in-situ section of oceanic Layer 3. In: *Proceedings of the Ocean Drill Program, Scientific Results*, 118, Von Herzen, RP, Robinson, PT (Eds.), Coll Station TX (Ocean Drill Program) 118, 439–538. https://doi.org/10.2973/odp.proc.sr.118.128.1991.

Dick, H.J.B., Natland, J.H., Alt, J.C., Bach, W., Bideau, D., Gee, J.S., Haggas, S., Hertogen, J.G.H., Hirth, G., Holm, P.M., Ildefonse, B., Iturrino, G.J., John, B.E., Kelley, D.S., Kikawa, E., Kingdon, A., Le Roux, P.J., Maeda, J., Meyer, P.S., Miller, D.J., Naslund, H.R., Niu, Y.-L., Robinson, P.T., Snow, J., Stephen, R.A., Trimby, P.W., Worm, H.-U., & Yoshinobu, A. (2000) A long in situ section of the lower ocean crust: results of ODP Leg 176 drilling at the Southwest Indian Ridge. *Earth and Planetary Science Letters*, 179, 31–51. https://doi.org/10.1016/S0012-821X(00)00102-3.

Dick, H.J.B., Ozawa, K., Meyer, P.S., Niu, Y., Robinson, P.T., Constantin, M., Hebert, R., Maeda, J., Natland, J.H., Hirth, J.G., & Mackie, S.M. (2002) Primary silicate mineral chemistry of a 1.5-km section of very slow spreading lower ocean crust: ODP Hole 753B, Southwest Indian Ridge. *Proceedings of the Ocean Drilling Program* 176, 1–61. https://doi.org/10.2973/odp.proc.sr.176.001.2002.

Dick, H.J.B., Schouten, H., Meyer, P.S., Gallo, D.G., Bergh, H., Tyce, R., Patriat, P., Johnson, K.T.M., Snow, J., & Fischer, A. (1991b) Tectonic evolution of the Atlantis II Fracture Zone. In: *Proceedings of the Ocean Drilling Program*, Scientific Results, 118, Von Herzen, RP, Robinson, PT (Eds.), Coll Station TX (Ocean Drill Program) 118, 359–398. https://doi.org/10.2973/odp.proc.sr.118.156.1991.

Dick, H.J.B., Tivey, M.A., & Tucholke, B.E. (2008) Plutonic foundation of a slow-spreading ridge segment: Oceanic core complex at Kane Megamullion, 23°30'N, 45°20'W. *Geochemistry, Geophysics, Geosystems*, 9(5). *Geochemistry, Geophysics, Geosystems*, 1(9). https://doi.org/10.1029/2007GC001645.

Dohmen, R., Becker, H.W., & Chakraborty, S. (2007) Fe-Mg diffusion in olivine I: Experimental determination between 700 and 1200°C as a function of composition, crystal

orientation and oxygen fugacity. *Physics and Chemistry of Minerals,* 34, 389–407. https://doi.org/10.1007/s00269-007-0157-7.

Donaldson, C.H. (1977) Laboratory Duplication of Comb Layering in Rhum Pluton. *Mineralogical Magazine,* 41, 323–336. https://doi.org/10.1180/minmag.1977.041.319.03.

Donaldson, C.H. (1976) An experimental investigation of olivine morphology. *Contributions to Mineralogy and Petrology*, 57, 187–213. https://doi.org/10.1007/BF00405225.

Donaldson, C.H. (1974) Olivine Crystal Types in Harrisitic Rocks of the Rhum Pluton and in Archean Spinifex Rocks. *GSA Bulletin*, 85(11), 1721–1726. https://doi.org/10.1130/0016-7606(1974)85<1721:OCTIHR>2.0.CO;2.

Dowty, E. (1980) Crystal Growth and Nucleation Theory and the Numerical Simulation of Igneous Crystallization. In: *Physics of Magmatic Processes*, Hargraves RB (Eds.), Princeton Univ Press: 419–486. https://doi.org/10.1515/9781400854493.419.

Drouin, M., Godard, M., Ildefonse, B., Bruguier, O., & Garrido, C.J. (2009) Geochemical and petrographic evidence for magmatic impregnation in the oceanic lithosphere at Atlantis Massif, Mid-Atlantic Ridge (IODP Hole U1309D, 30°N). *Chemical Geology,* 264, 71–88. https://doi.org/10.1016/j.chemgeo.2009.02.013.

Dunn, R.A., Toomey, D.R., Solomon, S.C. (2000) Three-dimensional seismic structure and physical properties of the crust and shallow mantle beneath the East Pacific Rise at 9°30'N. *Journal of Geophysical Research: Solid Earth*, 105, 23537–23555. https://doi.org/10.1029/2000JB900210.

Elthon, D. (1979) High magnesian liquids as the parental magma for ocean floor basalts. *Nature*, 278, 514–518. https://doi.org/10.1038/278514a0.

Escartín, J., Smith, D. K., Cann, J., Schouten, H., Langmuir, C. H. & Escrig, S. (2008) Central role of detachment faults in accretion of slow-spreading oceanic lithosphere. *Nature*, 455, 790–794. https://doi.org/10.1002/ 2014GC005269.

Faak, K., Gillis, K.M. (2016) Slow cooling of the lowermost oceanic crust at the fast-spreading East Pacific Rise. *Geology*, 44, 115–118. https://doi.org/10.1130/G37353.1.

1163 Faure, F., Schiano, P., Trolliard, G., Nicollet, C., & Soulestin, B. (2007) Textural evolution
1164 of polyhedral olivine experiencing rapid cooling rates. *Contributions to Mineralogy and*
1165 *Petrology*, 153, 405–416. https://doi.org/10.1007/s00410-006-0154-8.

1166 Faure, F., Trolliard, G., Nicollet, C., & Montel, J.-M. (2003) A developmental model of
1167 olivine morphology as a function of the cooling rate and the degree of undercooling.
1168 *Contributions to Mineralogy and Petrology,* 145, 251–263. https://doi.org/10.1007/s00410-
1169 003-0449-y.

1170 Feig, S.T., Koepke, J., & Snow, J.E. (2006) Effect of water on tholeiitic basalt phase
1171 equilibria: an experimental study under oxidizing conditions. *Contributions to Mineralogy*
1172 *and Petrology,* 152, 611–638. https://doi.org/10.1007/s00410-006-0123-2.

1173 Ferrando, C., Godard, M., Ildefonse, B., & Rampone, E. (2018) Melt transport and mantle
1174 assimilation at Atlantis Massif (IODP Site U1309): Constraints from geochemical modeling.
1175 *Lithos,* 323, 24-43. https://doi.org/10.1016/j.lithos.2018.01.012.

1176 Ferrando, C., Lynn, K.J., Basch, V., Ildefonse, B., & Godard, M. (2020). Retrieving
1177 timescales of oceanic crustal evolution at Oceanic Core Complexes: Insights from diffusion
1178 modelling of geochemical profiles in olivine. *Lithos*, 376–377, 105727.
1179 https://doi.org/10.1016/j.lithos.2020.105727.

1180 France, L., Ildefonse, B., Koepke, J. (2009) Interactions between magma and hydrothermal
1181 system in Oman ophiolite and in IODP Hole 1256D: fossilization of a dynamic melt lens at
1182 fast spreading ridges. *Geochemistry, Geophysics, Geosystems*, 10, Q10O19.
1183 https://doi.org/10.1029/2009GC002652.

1184 Gao, Y., Hoefs, J., Hellebrand, E., von der Handt, A., Snow, J. (2007) Trace element
1185 zoning in pyroxenes from ODP Hole 735B gabbros: diffusive exchange or synkinematic
1186 crystal fractionation? *Contributions to Mineralogy and Petrology*, 153, 429–442.
1187 https://doi.org/10.1007/s00410-006-0158-4.

1188 Ghiorso, M.S., & Sack, R.O. (1995) Chemical Mass Transfer in Magmatic Processes. IV.
1189 A Revised and Internally Consistent Thermodynamic Model for the Interpolation and
1190 Extrapolation of Liquid-Solid Equilibria in Magmatic Systems at Elevated Temperatures and
1191 Pressures. *Contributions to Mineralogy and Petrology,* 119, 197-212.
1192 https://doi.org/10.1007/BF00307281.

1193 Gillis, K., Snow, J., Klaus, A., & the Expedition 345 Scientists (2014) Proceedings of the
1194 Integrated Ocean Drilling Program, Initial Reports, vol. 345, *Integrated Ocean Drill Program*
1195 *Manage Int*, College Station, Tex. https://doi.org/10.2204/iodp.proc.345.101.2014.

1196 Godard, M., Awaji, S., Hansen, H., Hellebrand, E., Brunelli, D., Johnson, K., Yamasaki,
1197 T., Maeda, J., Abratis, M., Christie, D., Kato, Y., Mariet, C., Rosner, M., 2009. Geochemistry
1198 of a long in-situ section of intrusive slow-spread oceanic lithosphere: results from IODP Site
1199 U1309 (Atlantis Massif, 30°N Mid-Atlantic-Ridge). *Earth and Planetary Science Letters*,
1200 279, 110–122. https://doi.org/10.1016/j.epsl.2008.12.034.

1201 Gracia, E., Bideau, D., Hekinian, R., & Lagabrielle, Y. (1999) Detailed geological
1202 mapping of two contrasting second-order segments of the Mid-Atlantic Ridge between
1203 Oceanographer and Hayes fracture zones (33°30'N-35°N). *Journal of Geophysical Research:*
1204 *Solid Earth*, 104, 22903–22921. https://doi.org/10.1029/1999JB900161.

1205 Grove, T. L., Kinzler, R. J., & Bryan, W. B. (1992) Fractionation of Mid-Ocean Ridge
1206 Basalt (MORB). *Geophysical Monograph Series*, 71, 281–310.
1207 https://doi.org/10.1029/GM071p0281

1208 Hammer, J.E., & Rutherford, M.J. (2002) An experimental study of the kinetics of
1209 decompression-induced crystallization in silicic melt. *Journal of Geophysical Research: Solid*
1210 *Earth,* 107, B1. https://doi.org/10.1029/2001JB000281.

1211 Hersum, T., Hilpert, M., & Marsh, B. (2005) Permeability and melt flow in simulated and
1212 natural partially molten basaltic magmas. *Earth and Planetary Science Letters*, 237, 798–814.
1213 https://doi.org/10.1016/j.epsl.2005.07.008.

1214 Holness, M.B., Anderson, A.T., Martin, V.M., Maclennan, J., Passmore, E., &
1215 Schwindinger, K. (2007) Textures in partially solidified crystalline nodules: a window into
1216 the pore structure of slowly cooled mafic intrusions. *Journal of Petrology,* 48, 1243–1264.
1217 https://doi.org/10.1093/petrology/egm016.

1218 Husen, A., Almeev, R.R., & Holtz, F. (2016) The Effect of H_2O and pressure on multiple
1219 saturation and liquid lines of descent in basalt from the Shatsky Rise. *Journal of Petrology,*
1220 57, 309–344. https://doi.org/10.1093/petrology/egw008.

Jackson, M.D., Blundy, J., & Sparks, R.S.J. (2018) Chemical differentiation, cold storage and remobilization of magma in the Earth's crust. *Nature*, 564, 405–409. https://doi.org/10.1038/s41586-018-0746-2.

Jian, H., Singh, S.C., Chen, Y.J., & Li, J. (2017) Evidence of an axial magma chamber beneath the ultraslow- spreading Southwest Indian Ridge. *Geology*, 45, 143–14644. https://doi.org/10.1130/G38356.1.

John, B.E., Foster, D.A., Murphy, J.M., Cheadle, M.J., Baines, A.G., Fanning, C.M., & Copeland, P. (2004) Determining the cooling history of in situ lower oceanic crust-Atlantis Bank, SW Indian Ridge. *Earth and Planetary Science Letters,* 222, 145–160. https://doi.org/10.1016/j.epsl.2004.02.014.

Kelemen, P.B. (1990) Reaction between ultramafic rock and fractionating basaltic magma I. phase relations, the origin of calc-alkaline magma series, and the formation of discordant dunite. *Journal of Petrology*, 31, 51–98. https://doi.org/10.1093/petrology/31.1.51.

Kelley, D.S., & Fruh-Green, G.L. (2001) Volatile lines of descent in submarine plutonic environments: insights from stable isotope and fluid inclusion analyses. *Geochimica et Cosmochimica Acta*, 65, 3325–3346. https://doi.org/10.1016/S0016-7037(01)00667-6.

Kirkpatrick, R.J., Robinson, G.R., & Hays, J.F. (1976) Kinetics of Crystal Growth From Silicate Melts: Anorthite and Diopside. *Journal of Geophysical Research: Atmospheres*, 81(32), 5715-5720. https://doi.org/10.1029/JB081i032p05715.

Koepke, J., France, L., Müller, T., Faure, F., Goetze, N., Dziony, W., & Ildefonse, B. (2011) Gabbros from IODP Site 1256, equatorial Pacific: Insight into axial magma chamber processes at fast spreading ocean ridges. *Geochimica et Cosmochimica Acta*, 12, Q09014. https://doi.org/10.1029/2011GC003655.

Korenaga, J., Kelemen, P. B. (1997) Origin of gabbro sills in the Moho transition zone of the Oman ophiolite: Implications for magma transport in the oceanic lower crust. *Journal of Geophysical Research: Solid Earth*, 102, 27729-27749. https://doi.org/10.1029/97JB02604

Korenaga, J., Kelemen, P. B. (1998) Melt migration through the oceanic lower crust: a constraint from melt percolation modeling with finite solid diffusion. *Earth and Planetary Science Letters*, 156, 1-11. https://doi.org/10.1016/S0012-821X(98)00004-1

1250 Kvassnes, A., & Grove, T. (2008) How partial melts of mafic lower crust affect ascending
1251 magmas at oceanic ridges. *Contributions to Mineralogy and Petrology*, 156, 49–71.
1252 https://doi.org/10.1007/s00410-007-0273-x

1253 Langmuir, C.H. (1989) Geochemical consequences of in situ crystallization. *Nature*, 340,
1254 199-205. https://doi.org/10.1038/340199a0.

1255 Le Roux, V., Dasgupta, R., & Lee, C.T.A. (2011) Mineralogical heterogeneities in the
1256 Earth's mantle: Constraints from Mn, Co, Ni and Zn partitioning during partial melting. *Earth*
1257 *and Planetary Science Letters,* 307, 395–408. https://doi.org/10.1016/j.epsl.2011.05.014.

1258 Leuthold, J., Blundy, J.D., Holness, M.B., & Sides, R. (2014) Successive episodes of
1259 reactive liquid flow through a layered intrusion (Unit 9, Rum Eastern Layered Intrusion,
1260 Scotland). *Contributions to Mineralogy and Petrology,* 168, 1021.
1261 https://doi.org/10.1007/s00410-014-1021-7.

1262 Lissenberg, C.J., & Dick, H.J.B. (2008) Melt-rock reaction in the lower oceanic crust and
1263 its implications for the genesis of mid-ocean ridge basalt. *Earth and Planetary Science*
1264 *Letters,* 271, 311–325. https://doi.org/10.1016/j.epsl.2008.04.023.

1265 Lissenberg, C.J., & MacLeod, C.J. (2016) A reactive porous flow control on mid-ocean
1266 ridge magmatic evolution. *Journal of Petrology*, 57, 2195–2220.
1267 https://doi.org/10.1093/petrology/egw074.

1268 Lissenberg, C.J., MacLeod, C.J., & Bennett, E.N. (2019) Consequences of a crystal mush-
1269 dominated magma plumbing system: a mid-ocean ridge perspective. *Philosophical*
1270 *Transactions of the Royal Society A*, 377, 2139. https://doi.org/10.1098/rsta.2018.0014.

1271 Lissenberg, C.J., MacLeod, C.J., Howard, K.A., & Godard, M. (2013) Pervasive reactive
1272 melt migration through fast-spreading lower oceanic crust (Hess Deep, equatorial Pacific
1273 Ocean). *Earth and Planetary Science Letters,* 361, 436–447.
1274 https://doi.org/10.1016/j.epsl.2012.11.012.

1275 MacLeod, C.J., Dick, H.J.B., Blum, P., Abe, N., Blackman, D.K., Bowles, J.A., Cheadle,
1276 M.J., Cho, K., Ciazela, J., Deans, J.R., Edgcomb, V.P., Ferrando, C., France, L., Ghosh, B.,
1277 Ildefonse, B., Kendrick, M.A., Koepke, J., Leong, J.A.M., Liu, C., Ma, Q., Morishita, T.,
1278 Morris, A., Natland, J.H., Nozaka, T., Pluemper, O., Sanfilippo, A., Sylvan, J.B., Tivey,
1279 M.A., Tribuzio, R., & Viegas, G. (2017) Proceedings of IODP Expedition 360. *Proceedings*

of the Integrated Ocean Discovery Program 360. https://doi.org/10.14379/iodp.proc.360.103.2017.

MacLeod, C. J., Searle, R. C., Murton, B. J., Casey, J. F., Mallows, C., Unsworth, S. C., Achenbach, K.L. & Harris, M. (2009). Life cycle of oceanic core complexes. *Earth and Planetary Science Letters*, 287, 333–344. https://doi.org/10.1016/j.epsl.2009.08.016.

Martel, C. (2012) Eruption Dynamics Inferred from Microlite Crystallization Experiments: Application to Plinian and dome-forming eruptions of Mt Pelée (Martinique, Lesser Antilles). *Journal of Petrology*, 53(4), 699-725. https://doi.org/10.1093/petrology/egr076.

Mollo, S., & Hammer, J.E. (2017) Dynamic crystallization in magmas. In: Mineral reaction kinetics: Microstructures, textures, chemical and isotopic signatures, Heinrich W, Abart R (Eds). *EMU Notes in Mineralogy,* 16(12), 373–418. https://doi.org/10.1180/EMU-notes.16.12.

Mourey, A.J., Shea T. (2019) Forming olivine phenocrysts in basalt: a 3D characterization of growth rates in laboratory experiments. *Frontiers in Earth Science* 7, 300. https://doi.org/10.3389/feart.2019.00300.

Natland, J.H., Dick, H.J.B. (2001) Formation of the lower ocean crust and the crystallization of gabbroic cumulates at a very slowly spreading ridge. *Journal of Volcanology and Geothermal Research*, 110, 191–233. https://doi.org/10.1016/S0377-0273(01)00211-6.

Nielsen, T.F.D., Andersen, J.C.Ø., Holness, M.B., Keiding, J.K., Rudashevsky, N.S., Rudashevsky, V.N., Salmonsen, L.P., Tegner, C., & Veksler I.V. (2015) The Skaergaard PGE and Gold Deposit: the Result of in situ Fractionation, Sulphide Saturation, and Magma Chamber-scale Precious Metal Redistribution by Immiscible Fe-rich Melt. *Journal of Petrology,* 56(8), 1643–1676. https://doi.org/10.1093/petrology/egv049.

O'Driscoll, B. (2005) Textural equilibrium in magmatic layers of the syn-tectonic Lough Fee ultramafic intrusion, NW Connemara: implications for adcumulus mineral growth. *Irish Journal of Earth Science*, 23, 39–45.

O'Driscoll, B., Donaldson, C.H., Troll, V.R., Jerram, D.A., & Emeleus, C.H. (2007) An origin for harrisitic and granular olivine in the rum layered suite, NW Scotland: A crystal size distribution study. *Journal of Petrology*, 48, 253–270. https://doi.org/10.1093/petrology/egl059.

1310 O'Hara, M. J., & Fry, N. (1996) The Highly Compatible Trace Element Paradox-Fractional
1311 Crystallization Revisited. *Journal of Petrology*, 37, 859–890.
1312 https://doi.org/10.1093/petrology/37.4.859.

1313 O'Neill, H. S., & Jenner, F. E. (2012) The global pattern of trace element distributions in
1314 ocean floor basalts. *Nature*, 491, 698–705. https://doi.org/10.1038/nature11678.

1315 Rampone, E., Borghini, G., Godard, M., Ildefonse, B., Crispini, L., & Fumagalli, P. (2016)
1316 Melt/rock reaction at oceanic peridotite/gabbro transition as revealed by trace element
1317 chemistry of olivine. *Geochimica et Cosmochimica Acta*, 190, 309–331.
1318 https://doi.org/10.1016/j.gca.2016.06.029.

1319 Roeder, P.L., & Emslie, R.F. (1970) Olivine-liquid equilibrium. *Contributions to*
1320 *Mineralogy and Petrology*, 29, 277–302. https://doi.org/10.1007/BF00371276

1321 Ross, D.K., & Elthon, D. (1997) Cumulus and postcumulus crystallization in the oceanic
1322 crust: major- and trace-element geochemistry of Leg 153 gabbroic rocks. *Proceedings of the*
1323 *Ocean Drilling Program, Scientific Results,* 153, 333–353.
1324 https://doi.org/10.2973/odp.proc.sr.153.023.1997.

1325 Sanfilippo, A., Dick, H.J.B., & Ohara, Y. (2013) Melt-rock reaction in the mantle: mantle
1326 troctolites from the Parece Vela ancient back-arc spreading center. *Journal of Petrology*, 54,
1327 861–885. https://doi.org/10.1093/petrology/egs089.

1328 Sanfilippo, A., Tribuzio, R., & Tiepolo, M. (2014) Mantle-crust interactions in the oceanic
1329 lithosphere: Constraints from minor and trace elements in olivine. *Geochimica et*
1330 *Cosmochimica Acta,* 141, 423–439. https://doi.org/10.1016/j.gca.2014.06.012.

1331 Sanfilippo, A., Tribuzio, R., Tiepolo, M., & Berno, D. (2015) Reactive flow as dominant
1332 evolution process in the lowermost oceanic crust: evidence from olivine of the Pineto
1333 ophiolite (Corsica). *Contributions to Mineralogy and Petrology,* 170, 38.
1334 https://doi.org/10.1007/s00410-015-1194-8.

1335 Sanfilippo, A., MacLeod, C.J., Tribuzio, R., Lissenberg, C.J., & Zanetti, A. (2020) Early-
1336 stage melt-rock reaction in a cooling crystal mush beneath a slow-spreading mid-ocean ridge
1337 (IODP Hole U1473A, Atlantis Bank, Southwest Indian Ridge). *Frontiers in Earth Science,*
1338 provisionally accepted.

1339 Saper, L., & Liang, Y. (2014) Formation of plagioclase-bearing peridotite and plagioclase-
1340 bearing wehrlite and gabbro suite through reactive crystallization: an experimental study.
1341 *Contributions to Mineralogy and Petrology,* 167, 1–16. https://doi.org/10.1007/s00410-014-
1342 0985-7.

1343 Singh, S.C., Crawford, W.C., Carton, H., Seher, T., Combier, V., Cannat, M., Canales,
1344 J.P., Düsünür, D., Escartin, J., & Miranda, J.M. (2006) Discovery of a magma chamber and
1345 faults beneath a Mid-Atlantic Ridge hydrothermal field. *Nature*, 442, 1029–1032.
1346 https://doi.org/10.1038/nature05105.

1347 Sinha, M.C., Navien, D.A., MacGregor, L.M., Constable, S., Peirce, C., White, A.,
1348 Heinson, G., Inglis, M.A. (1997) Evidence for accumulated melt beneath the slow-spreading
1349 Mid-Atlantic Ridge. *Philosophical Transactions of the Royal Society of London,* 355, 1723.
1350 https://doi.org/10.1098/rsta.1997.0008.

1351 Sinton, J.M., & Detrick, R.S. (1992) Mid-Ocean Ridge Magma Chambers. *Journal of*
1352 *Geophysical Research: Solid Earth*, 97, 197–216. https://doi.org/10.1029/91JB02508.

1353 Shea, T., Hammer, J.E., Hellebrand, E., Mourey, A.J., Costa, F., First, E.C., Lynn, K.J., &
1354 Melnik, O. (2019) Phosphorus and aluminum zoning in olivine: contrasting behavior of two
1355 nominally incompatible trace elements. *Contributions to Mineralogy and Petrology* 174, 85.
1356 https://doi.org/10.1007/s00410-019-1618-y.

1357 Solano, J.M.S., Jackson, M.D., Sparks, R.S.J., & Blundy, J. (2014) Evolution of major and
1358 trace element composition during melt migration through crystalline mush: implications for
1359 chemical differentiation in the crust. *American Journal of Science*, 314, 895–939.
1360 https://doi.org/10.2475/05.2014.01.

1361 Suhr, G., Hellebrand, E., Johnson, K., & Brunelli, D. (2008) Stacked gabbro units and
1362 intervening mantle: A detailed look at a section of IODP Leg 305, Hole U1309D.
1363 *Geochemistry, Geophysics, Geosystems*, 9. https://doi.org/10.1029/2008GC002012.

1364 Sun, C., Graff, M., & Liang, Y. (2017) Trace element partitioning between plagioclase and
1365 silicate melt: The importance of temperature and plagioclase composition, with implications
1366 for terrestrial and lunar magmatism. *Geochimica et Cosmochimica Acta*, 206, 273–295.
1367 https://doi.org/10.1016/j.gca.2017.03.003.

Sun, C., & Liang, Y. (2012) Distribution of REE between clinopyroxene and basaltic melt along a mantle adiabat: Effects of major element composition, water, and temperature. *Contributions to Mineralogy and Petrology*, 163, 807–823. https://doi.org/10.1007/s00410-011-0700-x.

Sun, C., & Liang, Y. (2013) The importance of crystal chemistry on REE partitioning between mantle minerals (garnet, clinopyroxene, orthopyroxene, and olivine) and basaltic melts. *Chemical Geology*, 358, 23–36. https://doi.org/10.1016/j.chemgeo.2013.08.045.

Sun, C., & Liang, Y. (2014) An assessment of subsolidus re-equilibration on REE distribution among mantle minerals olivine, orthopyroxene, clinopyroxene, and garnet in peridotites. *Chemical Geology*, 372, 80–91. https://doi.org/10.1016/j.chemgeo.2014.02.014.

Sun, S-s., & McDonough, W.F. (1989) Chemical and isotopic systematics of oceanic basalts: implications for mantle composition and processes. *Geological Society, London, Special Publications*, 42, 313–345. https://doi.org/10.1144/GSL.SP.1989.042.01.19.

Teagle, D. A. H., Alt, J. C., Umino, S., Miyashita, S., Banerjee, N. R., Wilson, D. S., & the Expedition 309/312 Scientists (2006) Proceedings IODP, 309/312. Washington, DC: *Integrated Ocean Drilling Program* Management International, Inc. https://doi.org/10.2204/iodp.proc.309312.2006.

Tribuzio R, Tiepolo M, Vannucci R (2000) Evolution of gabbroic rocks of the Northern Apennine ophiolites (Italy): Comparison with the lower oceanic crust from modern slow-spreading ridges. In: Ophiolites and oceanic crust: new insights from field studies and the Ocean Drilling Program, Dilek Y, Moores EM, Elthon D, Nicolas A (Eds.), *Geological Society of America Special Papers*, 349, 129-138. https://doi.org/10.1130/0-8137-2349-3.129.

Tucholke BE, Lin J, Kleinrock MC, Tivey MA, Reed TB, Goff J, Jaroslow GE (1997) Segmentation and crustal structure of the western Mid-Atlantic Ridge flank, 25°25'-27°10' N and 0-29 m.y. *Journal of Geophysical Research: Solid Earth*, 102, 10203–10223. https://doi.org/10.1029/96JB03896.

Van den Bleeken, G., Müntener, O., & Ulmer, P. (2011) Melt variability in percolated peridotite: An experimental study applied to reactive migration of tholeiitic basalt in the upper mantle. *Contributions to Mineralogy and Petrology,* 161, 921–945. https://doi.org/10.1007/s00410-010-0572-5.

Van Orman, J.A., Cherniak, D.J., Kita, N.T. (2014) Magnesium diffusion in plagioclase: Dependence on composition, and implications for thermal resetting of the ^{26}Al-^{26}Mg early solar system chronometer. *Earth and Planetary Science Letters,* 385, 79–88. https://doi.org/10.1016/j.epsl.2013.10.026.

Vanko, D.A., Stakes, D.S. (1991) Fluids in Oceanic Layer 3: Evidence from Veined Rocks, Hole 735B, Southwest Indian Ridge. In: *Proceedings of the Ocean Drill Program, Scientific Results*, 118, Von Herzen, RP, Robinson, PT (Eds.), Coll Station TX (Ocean Drill Program), 181–215. https://doi.org/10.2973/odp.proc.sr.118.121.1991

Villiger, S., Ulmer, P., & Müntener, O., (2007) Equilibrium and fractional crystallization experiments at 0.7 GPa; the effect of pressure on phase relations and liquid compositions of tholeiitic magmas. *Journal of Petrology*, 48, 159–184. https://doi.org/10.1093/petrology/egl058.

Welsch, B., Faure, F., Famin, V., Baronnet, A., & Bachèlery, P. (2013) Dendritic crystallization: a single process for all the textures of olivine in basalts? *Journal of Petrology*, 54, 539–574. https://doi.org/10.1093/petrology/egs077.

Yang, A.Y., Wang, C., Liang, Y., & Lissenberg, C.J. (2019) Reaction between mid-ocean ridge basalt and lower oceanic crust: an experimental study. *Geochemistry, Geophysics, Geosystems*, 20, 4390-4407. https://doi.org/10.1029/2019GC008368.

Zhang, W.Q., Liu, C.Z., & Dick, H.J.B. (2020) Evidence for Multi-stage Melt Transport in the Lower Ocean Crust: Atlantis Bank Gabbroic Massif (IODP Hole U1473A, SW Indian Ridge). *Journal of Petrology*, egaa082. https://doi.org/10.1093/petrology/egaa082